Reviewed Preprint
v1 • February 24, 2026
Not revised

Reviewed Preprint
v2 • May 13, 2026
Revised by authors

For correspondence:
meytal.landau@desy.de

Competing interests: No competing interests declared

Funding: See page 32

Reviewing editor: Feng Ding, Clemson University, United States

RNA Selectively Modulates Activity of Virulent Amyloid PSMα3 and Host Defense LL-37 via Phase Separation and Aggregation Dynamics

Bader Rayan[1], Eilon Barnea[1], Rinat Indig[1], Christian F Pantoja[2], Jesse Gayk[3], Yael Lupu-Haber[4], Alexander Upcher[5], Amir Argoetti[1], Jacob Aunstrup Larsen[6], Alexander K Buell[6], Markus Zweckstetter[2,7], Meytal Landau[1,3,8,9]

[1]Department of Biology, Technion-Israel Institute of Technology, Haifa, Israel • [2]German Center for Neurodegenerative Diseases (DZNE), Göttingen, Germany • [3]CSSB Centre for Structural Systems Biology, Deutsches Elektronen-Synchrotron DESY, Hamburg, Germany • [4]The Life Sciences and Engineering Infrastructure Center, Technion-Israel Institute of Technology, Haifa, Israel • [5]Ilse Katz Institute for Nanoscale Science and Technology, Ben Gurion University of the Negev, Beersheba, Israel • [6]Department of Biotechnology and Biomedicine, Technical University of Denmark DTU, Kongens Lyngby, Denmark • [7]Department for NMR-based Structural Biology, Max Planck Institute for Multidisciplinary Sciences, Göttingen, Germany • [8]The Center for Experimental Medicine, Universitätsklinikum Hamburg-Eppendorf (UKE), Hamburg, Germany • [9]European Molecular Biology Laboratory (EMBL), Hamburg, Germany

eLife Assessment

This study presents **valuable** findings on the differential effects of RNA on the phase separation, aggregation dynamics, and bioactivity of PSMα3 and LL-37. The authors provide **solid** evidence from complementary biophysical and cell-based experiments that RNA influences peptide assembly and associated in vitro activities. The study is of interest for understanding interactions between amyloidogenic peptides and nucleic acids, although the physiological significance and some aspects of the mechanistic interpretation would benefit from further clarification.

https://doi.org/10.7554/eLife.109290.2.sa3

Abstract

Amyloids, classically associated with neurodegenerative disease, also play important roles in infection and immunity. Phenol-soluble modulins (PSMs) from *Staphylococcus aureus* are amyloid-forming virulence peptides that contribute to cytotoxicity, immune modulation, and biofilm stability. PSMα3 forms cross-α amyloid fibrils and shares sequence and α-helical self-assembly features with LL-37, a human host-defence peptide that forms non-amyloid α-helical assemblies. Here, we identify RNA as a context-dependent regulator of their assembly pathways and biological activity. RNA consistently reduces LL-37 cytotoxicity toward human cells without compromising its antibacterial function, suggesting a host-protective effect. In contrast, RNA preserves PSMα3 cytotoxic and antimicrobial activity over time by reshaping its assembly landscape, promoting liquid–liquid phase separation at low concentrations and stabilizing dynamic α-helical intermediates. At higher RNA concentrations, both peptides transition into distinct aggregated states, amorphous for LL-37 and fibrillar for PSMα3, correlating with divergent functional outcomes. The amyloid inhibitor EGCG abolishes the bioactivity of both peptides by redirecting assembly into non-functional aggregates, highlighting that activity depends on supramolecular architecture and reversibility rather than aggregation per se. Together, these findings establish

RNA as an environmental regulator of α-helical peptide assemblies and reveal phase transitions as tuneable determinants of peptide function, with implications for microbial virulence, innate immunity, and therapeutic intervention in infectious and protein-aggregation–associated diseases.

Introduction

Bacterial amyloids are proteins capable of forming ordered fibrils, playing a crucial role in biofilm stability, surface adherence, cell toxicity and immune responses[1–6]. These amyloids are vital for the survival and virulence of many bacteria, enabling them to colonize and persist in diverse environments[7,8]. Some examples of bacterial amyloids include the Csg and Fap proteins from *Enterobacteria* and *Pseudomonas* species[1,6,7,9–11], respectively, which play a role in biofilm stability. Staphylococcal phenol-soluble modulins (PSMs) are short peptides that are capable of forming amyloid structures[12–20] and perform multiple roles central to pathogenesis and immune evasion in *Staphylococcus aureus*[21–36]. In this context, defining PSMs as "functional amyloids" implies that amyloid formation can serve regulatory purposes, including controlled storage, stabilization, or spatial organization of bioactive molecules, as described for peptide hormones[37] and RNA-binding proteins[38,39]. Accordingly, amyloid assembly may function as a reversible structural state that modulates the availability and timing of virulence-associated activities.

Among bacterial amyloids, PSMα3 is notable for its strong cytotoxicity toward a broad range of microbial and human cell types[28,34,40–42] and for adopting a unique cross-α amyloid architecture, in which α-helices stack perpendicular to the fibril axis in paired sheets[14–16]. Recent studies on fibril-forming antimicrobial peptides have suggested a correlation between α-helical conformations in the solid state and cytotoxicity[43–47]. This observation parallels findings in human disease-associated amyloids, where α-helical oligomeric intermediates are widely considered to represent the toxic species[48–50]. Similarly, within the PSMα family, distinct amyloid polymorphs appear to encode different biological functions[31]: the metastable and reversible cross-α assemblies of PSMα3 enable dynamic switching between inactive and active states, whereas the more stable and irreversible cross-β fibrils formed by the homologous PSMα1 peptide[19,51] may contribute to robust biofilm architecture. In this framework, toxicity is proposed to arise from transient assembly intermediates along the fibrillation pathway rather than from the mature fibrils themselves[52].

PSMα3 shares self-assembly of α-helices with LL-37, a human host defence peptide[53–55], even though LL-37 is not an amyloid and does not form canonical cross-α or cross-β fibrils. Moreover, the LL-37 antimicrobial active core (residues 17–29) shows sequence similarity to PSMα3, and the formation of non-amyloid fibrils composed of densely packed cationic amphipathic α-helices[56]. The sequence and α-helices self-assembly similarities supported the hypothesis that PSMα3 might recapitulate functions of LL-37, and indeed, they share the activation of the signal inhibitory receptor on leukocytes-1 (SIRL-1) which is a negative regulator of myeloid cell function and dampens antimicrobial responses[57]. Such common functions might be related to molecular mimicry and the ability of bacterial peptides to hijack immunomodulation pathways[58]. Indeed, PSMαs interact with the formyl peptide receptor 2 (FPR2) on immune cells, initiating immune responses such as chemotaxis, phagocytosis, and the secretion of pro-inflammatory cytokines. These reactions are critical for recruiting and activating immune cells, thereby amplifying the inflammatory response[23,59–64].

LL-37 has been shown to bind RNA released from dying cells, forming stable complexes that protect the RNA from enzymatic degradation and promote its uptake by dendritic cells[65]. Once internalized, these RNA–LL-37 complexes activate Toll-like receptors (TLRs), triggering cytokine production and dendritic cell maturation[65,66]. Beyond LL-37, other human AMPs, such as β-defensins, also form higher-order assemblies that organize nucleic acids into nanostructures with defined periodicity. These nanocomplexes potently stimulate TLRs, highlighting that innate immune activation is influenced not only by ligand identity, but also by the nanoscale geometry and spatial organization of the complexes[67–69].

Interestingly, nucleic acid interactions also play a key role in the immune activation triggered by bacterial amyloids. For example, PSMs co-assemble with extracellular DNA (eDNA), and CpG-rich DNA specifically promotes PSMα3 fibrillation, forming co-aggregates that colocalize with DNA in biofilms. These complexes activate TLR pathways and induce anti-dsDNA autoantibody responses in mice[27]. Similar mechanisms are seen in *E. coli* and *Salmonella*, where curli fibers bind eDNA, enhance fibrillation, and engage TLRs signaling, also promoting autoimmunity[70,71]. These findings suggest that amyloid–DNA complexes in bacterial biofilms are not only structural components but also potent immunomodulators with potential links to autoimmunity.

Given their shared cationic, amphipathic α-helical character, but distinct amyloidogenic properties, we sought to examine whether RNA differentially influences the assembly landscapes and bioactivity of PSMα3 and LL-37. RNA is increasingly recognized as a key regulator of protein phase behaviour, capable of promoting liquid–liquid phase separation (LLPS), altering aggregation pathways, and reshaping supramolecular organization. LLPS is a fundamental mechanism of cellular organization, in which biomolecules demix into dynamic, membraneless compartments that regulate processes such as RNA metabolism, stress responses, and signal transduction[72–75]. Whether bacterial virulence-associated peptides are similarly governed by RNA-mediated phase behaviour remains largely unexplored.

To address this, we investigated how defined RNA species modulate the structural transitions, material properties, and bioactivity of PSMα3 and LL-37. In parallel, we examined the impact of epigallocatechin gallate (EGCG), a small-molecule assembly modulator widely studied as an amyloid inhibitor[32,76–78], to compare RNA-driven regulation with pharmacological redirection of peptide assembly. By integrating biophysical, structural, and cellular approaches, this work aims to define how environmental factors reshape α-helical peptide assemblies and thereby influence bacterial virulence and host-defence mechanisms.

Results

PSMα3 interacts with RNA in vitro

The interactions between PSMα3 and RNA were assessed using an Electrophoretic Mobility Shift Assay (EMSA), comparing the binding affinity of PSMα3 to single-stranded PolyA RNA and double-stranded Poly (AU) RNA. These RNAs were selected as simplified, well-defined model RNAs to probe general peptide–RNA interactions in an unbiased manner, as no prior information was available regarding whether such interactions occur, or which specific RNA species might be involved. The RNA molecules were labelled with the IR800CW fluorescent dye (as detailed in the Methods section). Freshly dissolved PSMα3, at varying concentrations, was incubated with each RNA type at a constant concentration for 30 minutes at 37°C. The EMSA results revealed that PSMα3 exhibits a stronger binding affinity to double-stranded Poly (AU) RNA, as evidenced by significant shifts at lower peptide concentrations compared to single-stranded Poly (A) (Fig. 1).

Quantification of free and shifted RNA band intensities revealed a progressive increase in the fraction of RNA bound as a function of peptide concentration for both RNA molecules (Fig. S1). Poly (AU) RNA reached saturation at lower PSMα3 concentrations than Poly (A), consistent with stronger apparent binding. Fitting the binding curves to a Hill model yielded an apparent dissociation constant (Kd) of 61.8 ± 1.6 μM for Poly (AU) and 94.5 ± 5.4 μM for Poly (A) (Fig. S1). Hill coefficients greater than 1 were obtained for both RNAs, consistent with cooperative binding behaviour. Based on these Kd differences, subsequent experiments focused on PSMα3 behaviour in the presence of double-stranded Poly (AU) RNA (hereafter referred to as RNA).

Non-monotonic turbidity response of PSMα3 to RNA

In order to assess the concentration-dependent effect of RNA on PSMα3 we used turbidity assays. The results showed that a 30 min co-incubation of 100 μM PSMα3 with varying concentrations of RNA displayed an increased turbidity up to 50 ng/μl, while higher RNA concentrations displayed a decrease in turbidity (Fig. S2). The decrease in particle size above 50 ng/μL can be a result of either the formation of smaller particles or aggregation into larger clusters, which can settle out of

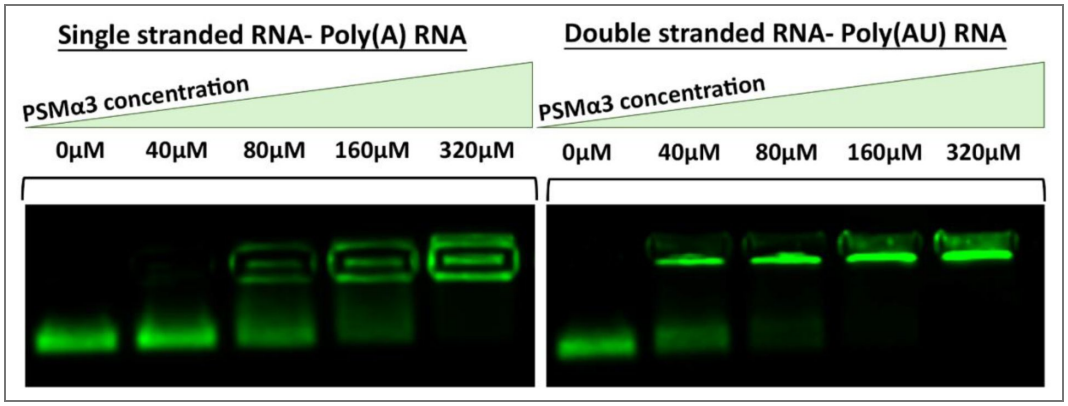

Figure 1. The binding and effect of single- and double-stranded RNA on PSMα3.

EMSA assay illustrating the interaction between PSMα3 and RNA. The assay compares the effects of increasing concentrations of PSMα3 (0 μM, 40 μM, 80 μM, 160 μM, and 320 μM), shown in a gradient from left to right, on the mobility shift of single-stranded Poly (A) RNA (left panel) and double-stranded Poly (AU) RNA (right panel) at ~400ng/μL.

suspension, removing them from the light-scattering medium and reducing turbidity. Alternatively, this non-monotonic turbidity behaviour is conceptually similar to charge-driven re-entrant transitions described in other protein–RNA phase-separating systems, such as Ddx4[79], however, the molecular context and assembly architecture of PSMα3 are fundamentally distinct. According to the turbidity results, we hypothesized that 50 ng/µl can be a critical concentration between soluble species, which might be able to phase separate, and the formation of aggregates.

RNA concentration regulates formation and liquid-to-solid transition of PSMα3 condensates

To better understand the nature of the PSMα3-RNA interaction, we visualized their mixtures via fluorescence microscopy, using PSMα3 labelled with Fluorescein isothiocyanate (FITC) at the C-terminus (PSMα3-FITC), which is known to form fibrils[14]. All fluorescence microscopy experiments used a mixture of 20% FITC-labelled and 80% unlabelled peptide to minimize potential effects of the fluorophore on assembly behaviour. 100 µM PSMα3-FITC was incubated with either 50 ng/µl or 400 ng/µl RNA, labelled using propidium iodide (PI), in a close to physiological buffer of 50 mM HEPES (pH 7.4) containing 150 mM sodium chloride (NaCl).

Upon addition of 50 ng/µL RNA, PSMα3 formed liquid–liquid phase-separated droplets that clearly colocalized with RNA (Fig. 2A). We further observed encapsulation of RNA within PSMα3–FITC–coated condensates (Fig. S3), indicating co-assembly rather than simple surface association. The liquid-like nature of these droplets was confirmed by fluorescence recovery after photobleaching (FRAP), which showed rapid signal recovery shortly after bleaching (Fig. 2B). Quantitative analysis revealed a half-time of recovery of 3.1 seconds and a mobile fraction of 68% (immobile fraction 32%) (Fig. S4), consistent with dynamic molecular exchange. Across multiple samples, we consistently observed coexistence of small droplets and larger aggregates. The experimental timescales examined do not allow us to reliably determine whether diffusion-driven coalescence kinetics would support classical droplet ripening dynamics[80,81]. Notably, after 2 hours of incubation, fluorescence recovery was no longer detected (Fig. 2C), indicating that the condensates undergo time-dependent aging and transition toward a more solid-like or aggregated state.

In contrast to the effect of 50 ng/µl RNA, the addition of a higher RNA concentration of 400 ng/µl to PSMα3 resulted in immediate aggregation, with no observed phase of droplet formation (Fig. 2D). FRAP analysis indicated no recovery of signal after bleaching, likely due to the formation of solid structures rather than droplets with liquid-like properties (Fig. 2E). In the absence of RNA, PSMα3 did not form condensates and instead appeared as dispersed or irregular assemblies (Fig. 2F), establishing that RNA is required to induce the droplet state observed under these conditions.

Colocalization between PSMα3-FITC and RNA was quantified using Pearson's correlation coefficient (above the Costes threshold) and Manders' overlap coefficients (tM1 and tM2) (Fig. S5). All metrics indicate substantially stronger spatial correlation and signal overlap at 50 ng/µL RNA compared with 400 ng/µL RNA. At low RNA concentration, Pearson's correlation is positive ($R \approx 0.53$), accompanied by high Manders' overlap values ($tM1 \approx 0.68$; $tM2 \approx 0.63$). This is consistent with coordinated association of PSMα3 and RNA within liquid-like droplets. In contrast, at 400 ng/µL RNA, Pearson's correlation becomes negative ($R \approx -0.24$) and Manders' coefficients are markedly reduced. This indicates a transition from co-localized droplet assemblies to spatially segregated aggregated structures in which RNA becomes partially excluded from the peptide-rich structures.

RNA concentration-driven changes in PSMα3 fibrillar morphology and aggregation

The TEM micrographs showed that in the absence of RNA, 100 µM PSMα3 formed nanotube-like fibrils after 2 hours, growing wider or with some twist after 24-hours co-incubation (Fig. 3A). Incubating PSMα3 with a low concentration of 10 ng/µL RNA displayed accelerated fibril

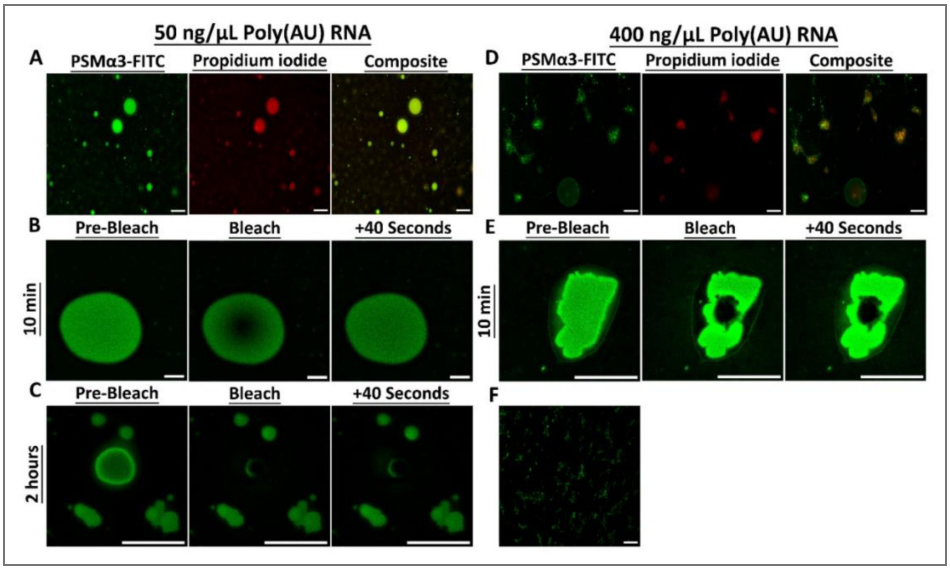

Figure 2. Colocalization, droplet formation, and texture of PSMα3 mixed with varying Poly (AU) RNA concentrations.

Widefield fluorescence microscopy images of 100 µM of 20% FITC-PSMα3 (green) and 80% unlabelled PSMα3 incubated with Poly (AU) RNA (red) at 50 ng/µL (**A**) or 400 ng/µL (**D**), shown as individual fluorescence channels and merged images. (**B-C**) FRAP analysis of PSMα3-FITC in the presence of 50 ng/µL Poly (AU) RNA after 10 min (**B**) or 2 h (**C**) of co-incubation. (**E**) FRAP analysis of PSMα3-FITC in the presence of 400 ng/µL Poly (AU) RNA after 10 min of co-incubation. For panels B, C, and E, images were acquired before photobleaching, immediately after photobleaching, and 40 s post-photobleaching. (**F**) 100 µM of 20% FITC-PSMα3 (green) and 80% unlabelled PSMα3 in the absence of RNA. All scale bars represent 20 µm.

formation, with more strongly twisted, wide, sheet-like fibrils observed after both 2 hours and 24 hours (Fig. 3A). With the addition of 50 ng/μL RNA, PSMα3 fibrils have a similar twisted morphology after 2 hours, while at a longer incubation time of 24 hours, we observed a significant morphological shift into more thin amorphous aggregates (Fig. 3A). At the higher concentration of 400 ng/μL RNA, PSMα3 formed dense, thin fibrils after 2 hours, but with a possible fragmentation into smaller species or rearrangement into amorphous aggregates after 24 hours of co-incubation. This indicates that RNA concentration and time of co-incubation affect the density and morphology of PSMα3 fibrils. This corresponds to the differences observed by light microscopy of co-aggregates contexture of LLPS droplets vs solid aggregates (Fig. 2).

These observations were further supported by TIRF microscopy using the amyloid-specific dye AmyTracker630 (AT630). With the addition of 50 ng/μL RNA to PSMα3-FITC, a strong AT630 fluorescence signal was detected only after 2 hours of co-incubation, but not after 30 minutes (Fig. 3B, quantified in Fig. S6). This suggests a time-dependent transition into amyloid-like species. Conversely, at 400 ng/μL RNA, a significant AT630 fluorescence was observed already after 30 minutes of co-incubation, consistent with a rapid formation of amyloid fibrils (Figs. 3C and S6). These findings highlight a concentration- and time-dependent modulation of PSMα3 phase separation and structural transitions, where RNA promotes LLPS at lower concentrations and drives rapid amyloid formation and unique fibrillar morphologies at higher concentrations. Future work will be required to quantitatively define the phase boundaries and delineate the dominant mechanisms, such as sedimentation, dissolution, or coarsening/aging, across intermediate RNA concentrations.

RNA enhances α-helical structure of PSMα3

Solid-state circular dichroism (ssCD) spectroscopy reveals that PSMα3 lacks a defined secondary structure both immediately after preparation and following 2 hours of incubation (Fig. S7). However, an α-helical signature of PSMα3 is markedly enhanced in the presence of RNA compared to peptide alone, as evidenced by increased signal intensity, deeper minima, and more pronounced spectral features characteristic of α-helical structure. This enhancement is more pronounced at 400 ng/μL RNA than at 50 ng/μL, particularly after 2 hours of co-incubation, indicating that RNA concentration influences the stabilization of α-helical assemblies. This supports the notion that RNA not only accelerates aggregation but also promotes or stabilizes the α-helical fibrillar architecture, potentially consistent with cross-α amyloid structures.

RNA modulates the antibacterial activity of PSMα3

The antimicrobial activity of PSMα3 against *Escherichia coli* was evaluated under varying RNA concentrations and incubation times using the PrestoBlue Cell Viability Assay (Fig. 4A). Freshly dissolved 10 or 20 μM PSMα3 exhibited potent antibacterial activity, completely abolishing bacterial viability. After 2 hours of incubation, PSMα3 retained its full activity, comparable to its freshly prepared state. The presence of RNA at 50 ng/μL and 400 ng/μL had no impact on its antimicrobial function within this timeframe (Fig. 4A).

In contrast, after 24 hours of incubation, PSMα3's antibacterial activity was significantly reduced (Fig. 4A), suggesting a decrease in its effective concentration or changes in its morphology. Notably, the addition of RNA at 50 ng/μL or 400 ng/μL prevented this loss of activity, indicating that RNA plays a stabilizing role in toxic species or their reservoir. These findings suggest that RNA influences PSMα3 aggregation dynamics and morphology, thereby modulating its long-term antimicrobial effectiveness.

RNA modulates PSMα3 cytotoxicity against human HeLa cells

The effect of RNA on the cytotoxicity of PSMα3 against human HeLa cells was evaluated by measuring lactate dehydrogenase (LDH) release, an indicator of cell membrane damage (Fig. 4B). Freshly dissolved PSMα3 exhibited substantial cytotoxicity, causing approximately 80% cell death at 20 μM and 50% at 10 μM. The presence of RNA did not significantly alter the toxicity of freshly dissolved PSMα3 (Fig. 4B), similar to the antibacterial activity. However, following 2

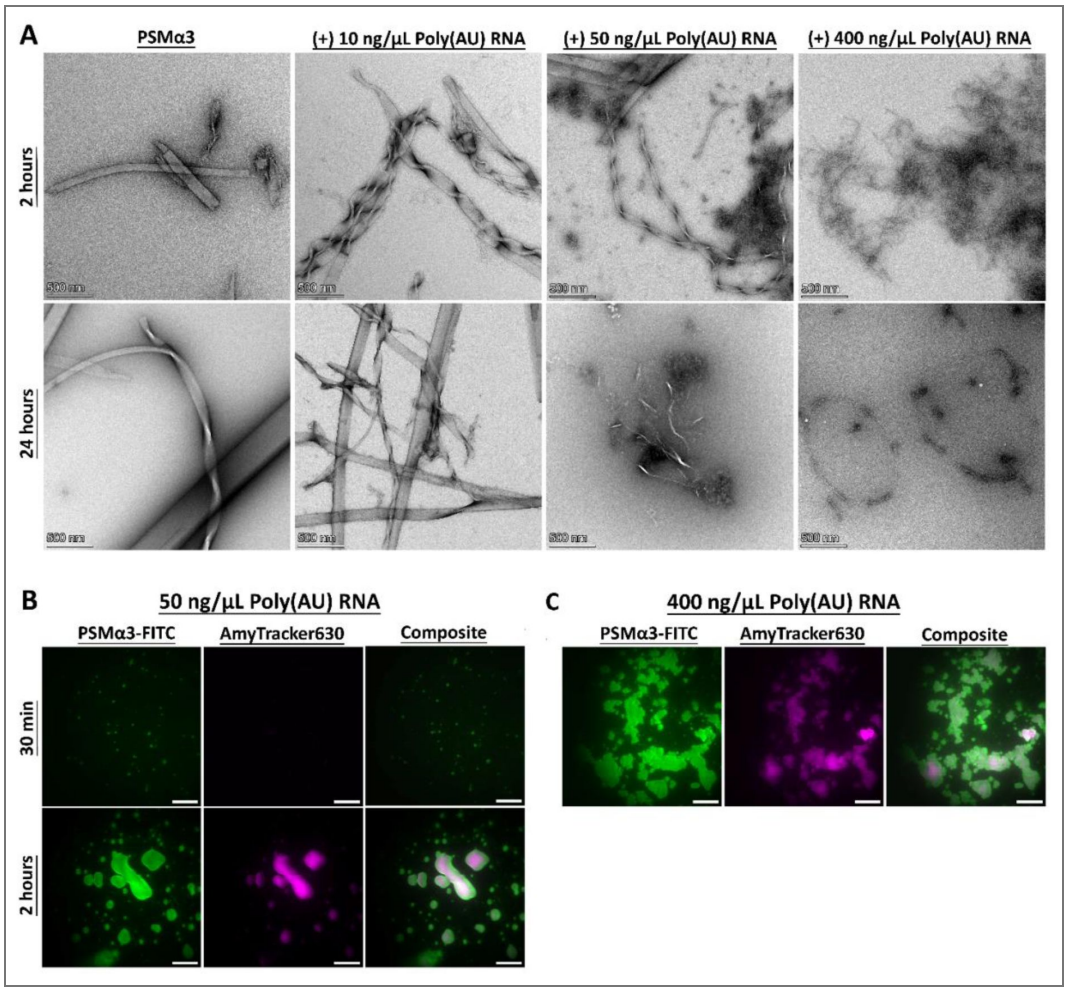

Figure 3. TEM and TIRF visualization of PSMα3 aggregation and morphology with different Poly (AU) RNA concentrations and incubation times.

(A) TEM micrographs of 100 μM PSMα3 incubated with or without Poly (AU) RNA at varying concentrations of 10 ng/μL, 50 ng/μL, and 400 ng/μL for 2 hours (top row) and 24 hours (bottom row). Scale bars represent 500 nm. **(B)** TIRF microscopy images showing 100 μM of 20% FITC-PSMα3 (green) and 80% unlabelled PSMα3 co-incubated with 50 ng/μL Poly (AU) RNA and the amyloid indicator AT630 (magenta) for 30 minutes and 2 hours. Scale bars represent 20 μm. **(C)** TIRF microscopy images of 100 μM of 20% FITC-PSMα3 (green) and 80% unlabelled PSMα3 co-incubated with 400 ng/μL Poly (AU) RNA and AT630 (magenta) for 30 min. Scale bars represent 20 μm.

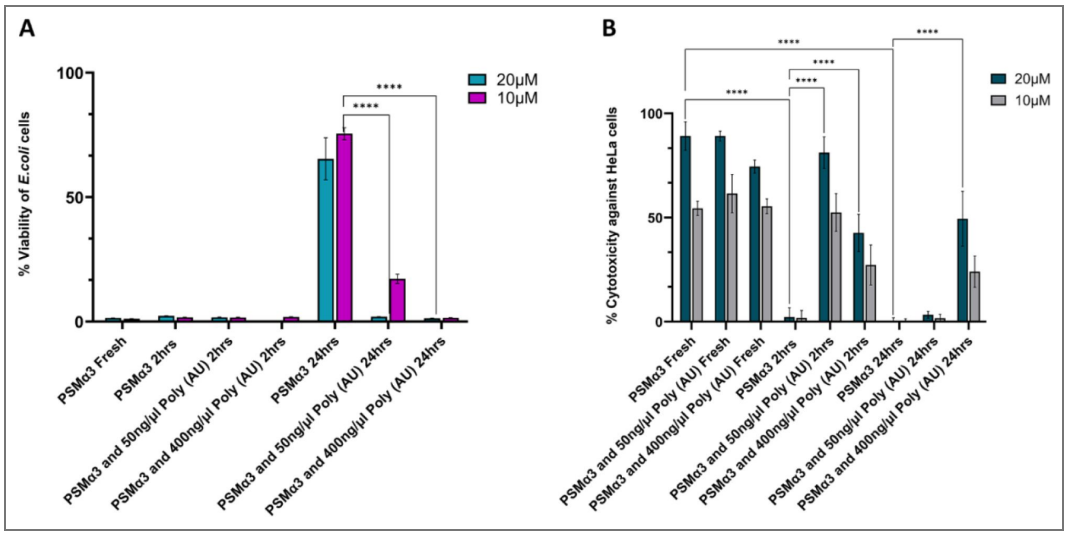

Figure 4. Impact of Poly (AU) RNA on PSMα3 cytotoxicity and antibacterial activity.

Antimicrobial activity of PSMα3 against *E. Coli* using the PrestoBlue cell viability assay (**A**) and its cytotoxicity against HeLa cells using the LDH colorimetric assay (**B**) were assessed with and without Poly (AU) RNA at varying concentrations. The experiments were performed in at least three replicates and repeated across three independent days to ensure result reliability. Cytotoxicity and bacterial cell viability percentages were calculated as the mean of all replicates, with error bars representing the standard error of the mean (SEM). Statistical significance was determined using one-way ANOVA for normally distributed data in GraphPad Prism (version 11). Significance levels are indicated as follows: *p<0.05, **p<0.01, ***p<0.001, ****p<0.0001.

hours of incubation, PSMα3 cytotoxicity was significantly reduced, possibly due to aggregation and a loss of active peptide concentration. This reduction occurred earlier than the loss of antibacterial activity, which was only observed after 24 hours of incubation (Fig. 4A).

Notably, co-incubation with RNA helped maintain PSMα3 cytotoxicity in a concentration-dependent manner. With 50 ng/μL RNA, the 2-hour incubated PSMα3 retained cytotoxicity comparable to its freshly dissolved form, suggesting that RNA prevents activity loss due to incubation. However, after 24 hours, 50 ng/μL RNA was insufficient to preserve cytotoxicity. In contrast, at 400 ng/μL RNA, partial cytotoxicity was maintained for both 2-hour and 24-hour incubated PSMα3, compared to the freshly dissolved sample.

Overall, these findings suggest that RNA prevents the incubation-induced loss of both antibacterial activity and cytotoxicity (Fig. 4). This effect appears to be concentration- and co- incubation time-dependent, likely linked to RNA-induced morphological variations of PSMα3 species (Figs. 2-3).

PSMα3 targets nucleolar nucleic acids in HeLa cells with LLPS dynamics

The interactions and localization of PSMα3 were next explored in HeLa cells with the addition of 20μM PSMα3 just before imaging. PI was added to the cell medium as a marker for cell death, as it selectively penetrates dead cells and binds to their nucleic acids.

Confocal microscopy images revealed that PSMα3 induces significant toxicity as indicated by membrane damage and blebbing, intracellular PSMα3 aggregate formation, and positive PI staining (Fig. 5 and Movie. S1). PSMα3 also enters the nuclei, with a notable concentration in the nucleolus, indicated by the foci of green fluorescence (marked by white arrows in Fig. 5). The composite images demonstrated clear colocalization of PSMα3 with nucleic acids in the nucleolus, as seen by the overlap of the green PSMα3-FITC signal and the red fluorescence from PI-stained nucleic acids.

FRAP analysis of 20 μM PSMα3 within the nucleolus of HeLa cells revealed measurable but constrained mobility (Fig. 5B). Following photobleaching of a defined nucleolar region (indicated by the white arrow), fluorescence gradually recovered over the 60 s acquisition window, indicating dynamic exchange of PSMα3 within this compartment. However, recovery was slow and incomplete during this time frame, and did not reach a clear plateau, precluding reliable determination of recovery half-time or precise mobile and immobile fractions (Fig. S8), and indicating dynamic but constrained exchange within this RNA-rich compartment. This behaviour differs from the rapid and near-complete recovery observed for PSMα3–RNA droplets formed in vitro (Fig. 2C), indicating that nucleolar-associated PSMα3 exhibits more restricted dynamics than liquid-like condensates in defined buffer systems.

EGCG directly binds PSMα3 and inhibits its fibrillation and bioactivity, even in the presence of RNA

Since RNA appears to protect or maintain PSMα3's toxic functions, potentially by influencing its fibril formation and morphology, we investigated the corresponding and combined effects of an inhibitor of fibril formation. One such inhibitor is epigallocatechin gallate (EGCG), the most abundant catechin in tea and a known amyloid inhibitor, including PSMs[32].

The addition of EGCG to PSMα3 at a 1:1 molar ratio did not significantly alter its cytotoxicity against HeLa cells. However, at a fivefold molar excess, EGCG completely abolished PSMα3's cytotoxic effect (Fig. 6A). To examine the structural changes underlying this effect, we analysed fibril formation kinetics and morphology in the presence of EGCG. TEM micrographs revealed that a fivefold molar excess of EGCG disrupted fibril formation of 100 μM PSMα3, instead inducing amorphous aggregates (Fig. 6B). Consistently, kinetics assays of fibril formation showed that EGCG inhibited the ThT fluorescence curve otherwise indicating the fibril formation of 100 μM PSMα3 (Fig. S9). These findings suggest that EGCG reduces PSMα3 toxicity by modulating its

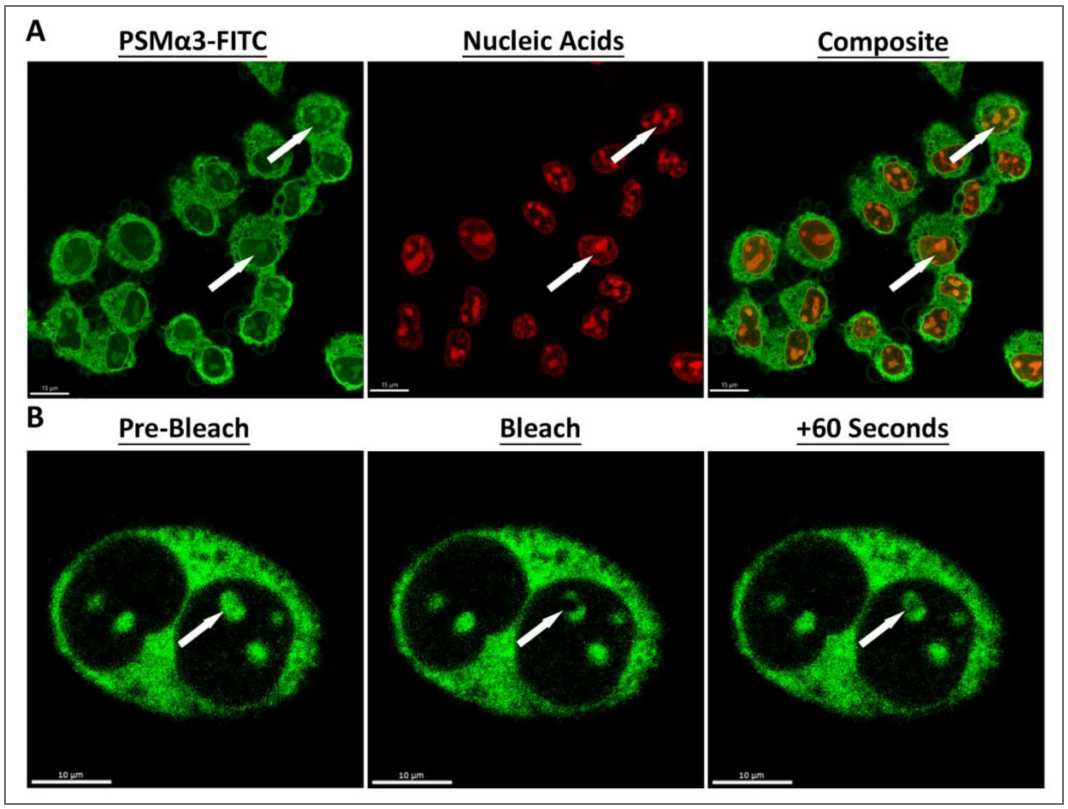

Figure 5. Colocalization of PSMα3 with nucleic acids in HeLa cells.

(A) Confocal microscopy images showing the localization and colocalization of 20 μM of 20% FITC-PSMα3 (green) and 80% unlabelled PSMα3 and nucleic acids stained with PI (red) inside the nucleolus of HeLa cells (indicated in arrows). The left panel illustrates the distribution of PSMα3 within the cell. The middle panel shows the nucleic acids stained with PI. The right panel is a composite image that demonstrates the colocalization of PSMα3 with nucleic acids. Scale bars represent 15 μm. **(B)** FRAP analysis of 20 μM of 20% FITC-PSMα3 (green) and 80% unlabelled PSMα3 inside the nucleolus (indicated by the arrow) of HeLa cells, showing fluorescence recovery after 60 seconds. Scale bars represent 10 μm.

fibril formation and morphology. The addition of RNA did not counteract the effect of EGCG or restore PSMα3 cytotoxicity (Fig. 6A), highlighting the strong impact of EGCG on PSMα3 morphology and properties.

Live-cell confocal microscopy provided further insights into how EGCG binding affects PSMα3 interactions with cells. In accordance with the LDH measurements (Fig. 6A), in the absence of EGCG, 20 μM PSMα3 readily penetrated cells and induced robust PI staining, indicating membrane disruption (Fig. 6C, top panel and Movie. S1). In contrast, a fivefold molar excess of EGCG prevented the toxic effects of 20 μM PSMα3, blocking cell penetration and PI staining (Fig. 6C, bottom panel and Movie. S2). Instead, PSMα3-FITC formed extracellular aggregates and showed no interaction with cell membranes, as indicated by the absence of PI staining and intact cell membranes.

Furthermore, EGCG at a fivefold molar excess also reduced the antibacterial activity of PSMα3 against *E. coli*, maintaining bacterial cell viability (Fig. S10). Super-resolution fluorescence microscopy showed that while 20 μM PSMα3 typically aggregates on the bacterial membrane, causing membrane disruption and PI staining indicative of cell death (Fig. S10), EGCG at a fivefold molar excess prevented membrane aggregation and PI staining, thereby preserving membrane integrity.

To investigate residue-specific interactions between PSMα3 and EGCG, we performed NMR spectroscopy using a 2:1 PSMα3:EGCG molar ratio. The 1D 1H-NMR spectrum revealed distinct chemical shift changes and peak broadening upon EGCG addition, particularly in residues Met1, Glu2, and V4/N21, suggesting specific interactions between these sites and the EGCG molecule (Fig. 7A). Peak broadening was also observed in the aromatic region of EGCG, especially for protons H1 and H2, compared to the reference spectrum of EGCG alone, indicating that the interaction is visible from the EGCG side as well. Notably, slight opalescence was observed in the sample following preparation, potentially reflecting early-stage aggregate formation. Additionally, the presence of multiple cross-peaks between non-sequential residues (i+3 or i+4) in the two-dimensional (2D) ^{1}H-^{1}H Nuclear Overhauser Effect Spectroscopy (NOESY) spectrum indicates a well-defined structure of PSMα3 in this condition (Fig. 7B). The 2D ^{1}H-^{1}H Total Correlation Spectroscopy (TOCSY) spectrum displayed connectivity between backbone amide (HN) and alpha protons (Hα) for several assigned residues, while the 2D ^{1}H-^{1}H NOESY spectrum revealed spatial correlations between nearby residues (i+1).

To assess the temporal stability of the sample, we monitored signal intensities over a 3-day period. PSMα3 signals remained stable, with only a ~10% decrease in intensity, whereas EGCG signals exhibited substantial degradation, with nearly 50% loss over the same time frame (Fig. 7C). Given the ~1.5-day duration of the 2D NMR measurements, it is estimated that over 60% of EGCG remained in solution during data acquisition, allowing for reliable observation of its interaction with the peptide. Of note, EGCG's activity has been shown to depend on its chemical stability and the surrounding conditions. Specifically, at neutral pH, EGCG may undergo oxidation, and its inhibitory effects could be attributed to its degradation products rather than the intact compound itself[82].

RNA modulates the human host defence peptide LL-37 phase behaviour and cytotoxicity without compromising antimicrobial activity

LL-37, a human host defence peptide, shares similarities with PSMα3, including its ability to self-assemble into α-helical supramolecular structures and to interact with nucleic acids[56,65]. We therefore examined whether RNA similarly influences LL-37 activity and properties.

Fluorescence microscopy showed that 100 μM LL-37-FITC incubated with 100 ng/μL PI-labelled Poly (AU) RNA formed aggregates, with no evidence of droplet formation or LLPS under these conditions (Fig. S11). Because diverse cellular stresses are known to induce condensation of RNA-binding proteins and promote the formation of stress-associated assemblies[83], we next examined the effect of RNA on LL-37 under thermal stress. Following heat shock at 65 °C for 15

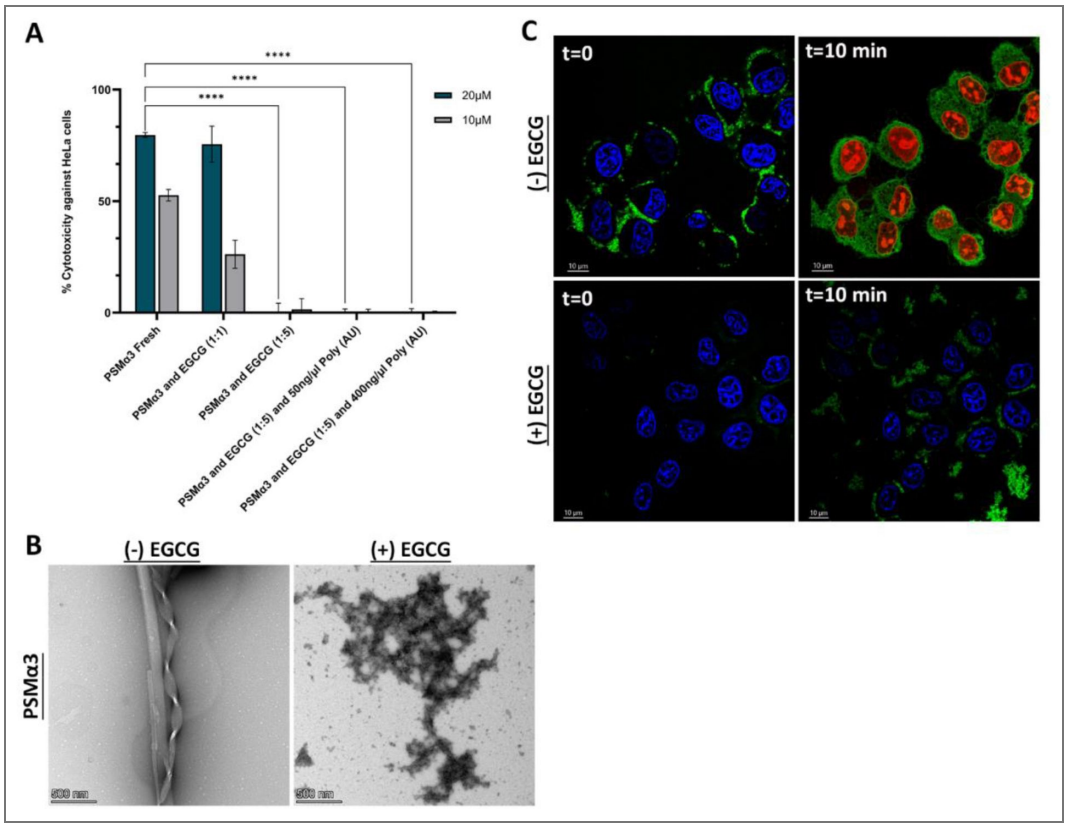

Figure 6. EGCG modulates PSMα3 aggregation and reduces toxicity against HeLa cells.

(**A**) Cytotoxicity of PSMα3 against HeLa cells in the presence and absence of EGCG and Poly (AU) RNA at two different concentrations, assessed via LDH assay. The experiment was performed in triplicate and repeated on three separate days for consistency. Cytotoxicity percentages were averaged across all replicates, with error bars representing the standard error of the mean. Statistical significance: *p < 0.05, **p < 0.01, ***p < 0.001, ****p < 0.0001 (one-way ANOVA, GraphPad Prism v11). (**B**) TEM micrographs of 100 μM PSMα3 incubated for 24 hours, without (left) and with (right) a fivefold molar excess of EGCG. Scale bars: 500 nm. (**C**) Live-cell confocal microscopy of HeLa cells treated with 20 μM of 20% FITC-PSMα3 (green) and 80% unlabelled PSMα3 without (top) and with EGCG (bottom), imaged immediately after preparation (t = 0) and after 10 minutes. Hoechst 33342 (blue) marks the nuclei, while PI staining (red) indicates membrane disruption. Scale bars: 10 μm.

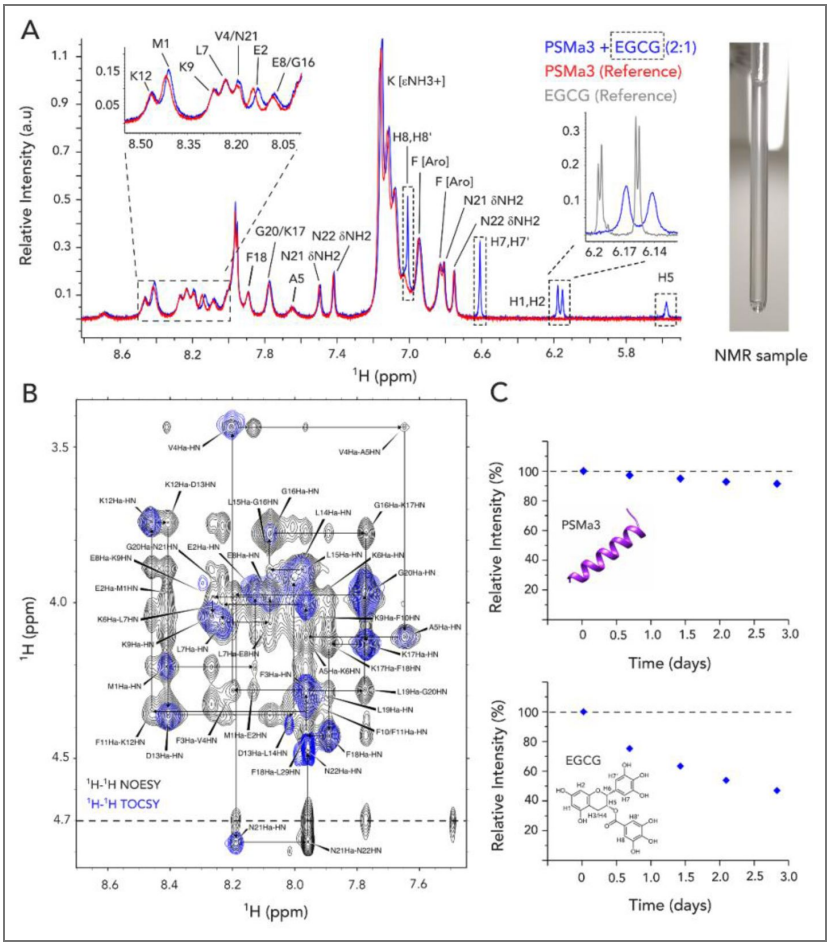

Figure 7. Residue-specific interactions between PSMα3 and EGCG.

(**A**) One-dimensional (1D) ^{1}H NMR spectra of 1.0 mM PSMα3 alone (red) and in complex with 0.5 mM EGCG (blue), recorded at 35 °C. Specific residues, including Met1, Glu2 and V4/N21, show chemical shift changes suggestive of direct interaction with EGCG (highlighted in the upper left). Dashed boxes mark proton signals corresponding to EGCG. Peak broadening of H1/H2 protons, compared to the EGCG-only reference sample (light grey), indicates interaction from the EGCG side. Slight opalescence observed in the sample suggests potential aggregate formation. (**B**) Two-dimensional (2D) ^{1}H–^{1}H TOCSY and NOESY spectra of the PSMα3:EGCG complex at a 2:1 ratio, recorded at 35 °C. The cross-peaks in the TOCSY spectrum allow the identification of the spin system and direct connections through the scalar coupling between the proton amide (HN) and the alpha protons (Hα) of the same residue. The cross-peaks in the NOESY spectrum establish a sequential connection between neighbouring residues (i+1), allowing spectral assignment. The remaining cross-peaks (i+3 or i+4) in the spectrum support PSMα3 secondary structure in the experimental conditions. (**C**) Temporal stability of the PSMα3:EGCG sample over 3 days.

minutes, RNA markedly altered LL-37 assembly behaviour in a concentration-dependent manner. At 100 ng/μL RNA, LL-37 formed rounded condensates that colocalized with RNA (Fig. 8A). To assess the material properties of these assemblies, we performed FRAP analysis on LL-37–FITC under this condition. Photobleaching resulted in minimal fluorescence recovery over the acquisition window (Fig. S12), indicating that the LL-37–RNA assemblies formed after heat shock are predominantly solid-like rather than liquid-like. At 200 ng/μL RNA, LL-37 assemblies exhibited mixed features, with rounded structures still present but accompanied by increasing aggregation, consistent with a transition toward a more solid state (Fig. 8B). At 400 ng/μL RNA, discrete condensates were no longer observed and LL-37 instead formed extensive, irregular aggregates with strong RNA colocalization (Fig. 8C).

For comparison, PSMα3 subjected to the same heat-shock protocol exhibited droplet formation only under more permissive conditions (pH 4), but not at physiological pH (7.4) (Figs. S13-S14). Together, these results indicate that, for both LL-37 and PSMα3, increasing RNA concentration favours aggregation over phase separation, and that LL-37 assemblies formed under thermal stress rapidly adopt solid-like properties rather than maintaining liquid-like dynamics.

Freshly dissolved LL-37 exhibited cytotoxicity against HeLa cells, which, in contrast to PSMα3, remained consistent even after incubation for up to 24 hours. Notably, RNA significantly reduced LL-37 cytotoxicity in a concentration-dependent manner, irrespective of the incubation duration (freshly dissolved, 2 hours, or 24 hours) (Fig. 8D). This contrasts with RNA's rescuing effect on the incubation time-dependent loss of PSMα3 cytotoxicity. The antimicrobial activity of LL-37 against *E. coli* also remained unchanged upon incubation. However, unlike its effect on cytotoxicity, RNA had minimal impact on antibacterial activity, with only high concentrations of 400 ng/μL reducing LL-37 activity (Fig. 8E). Similar to PSMα3, LL-37 cytotoxicity against HeLa cells and its antimicrobial activity were attenuated by EGCG in a concentration-dependent manner (Fig. 8E).

TEM micrographs of 100 μM LL-37 revealed a variety of aggregative and fibrous structures, including thin, curli-like fibrils, although no consistent morphology was observed (Fig. S15A). RNA induced a distinct morphological change, leading to increased aggregation and the formation of mostly amorphous species, but also some thicker, ribbon-like fibrils were observed. These structures resemble those previously observed for a segment of the LL-37 active core (residues 17–29), which is similar to PSMα3 in sequence and its ability to form fibrils of densely packed amphipathic α-helices[56]. Heat shock further intensified aggregation, resulting in denser, amorphous condensates and larger fibrillar assemblies, with and without RNA (Fig. S15B). The distinct effects of RNA on the aggregation and morphologies of LL-37 and PSMα3 may underlie the observed differences in their cytotoxic and antibacterial activities.

Discussion

This study identifies RNA as a context-dependent regulator of α-helical assembly-prone peptides, demonstrating that RNA reshapes their supramolecular landscape and thereby tunes bioactivity rather than merely sequestering peptide species. This is supported by the emergence of distinct RNA-dependent material states (from droplets to aged solids) and RNA-dependent fibrillar morphologies with divergent activity profiles across time and concentration. By comparing the bacterial virulence factor PSMα3, which forms canonical cross-α amyloid assemblies, with the human host-defence peptide LL-37, which forms α-helical fibrils but lacks amyloid-like stacking, we reveal that RNA differentially modulates structurally distinct systems through peptide-specific effects on phase behaviour and aggregation dynamics.

Toxicity and antibacterial activity arise from dynamic intermediates

Our data support a model in which PSMα3 toxicity does not arise from a single static species, such as monomers or mature fibrils, but from dynamic assembly processes that include transient α-helical assembly intermediates along the fibrillation pathway. While soluble species mediate

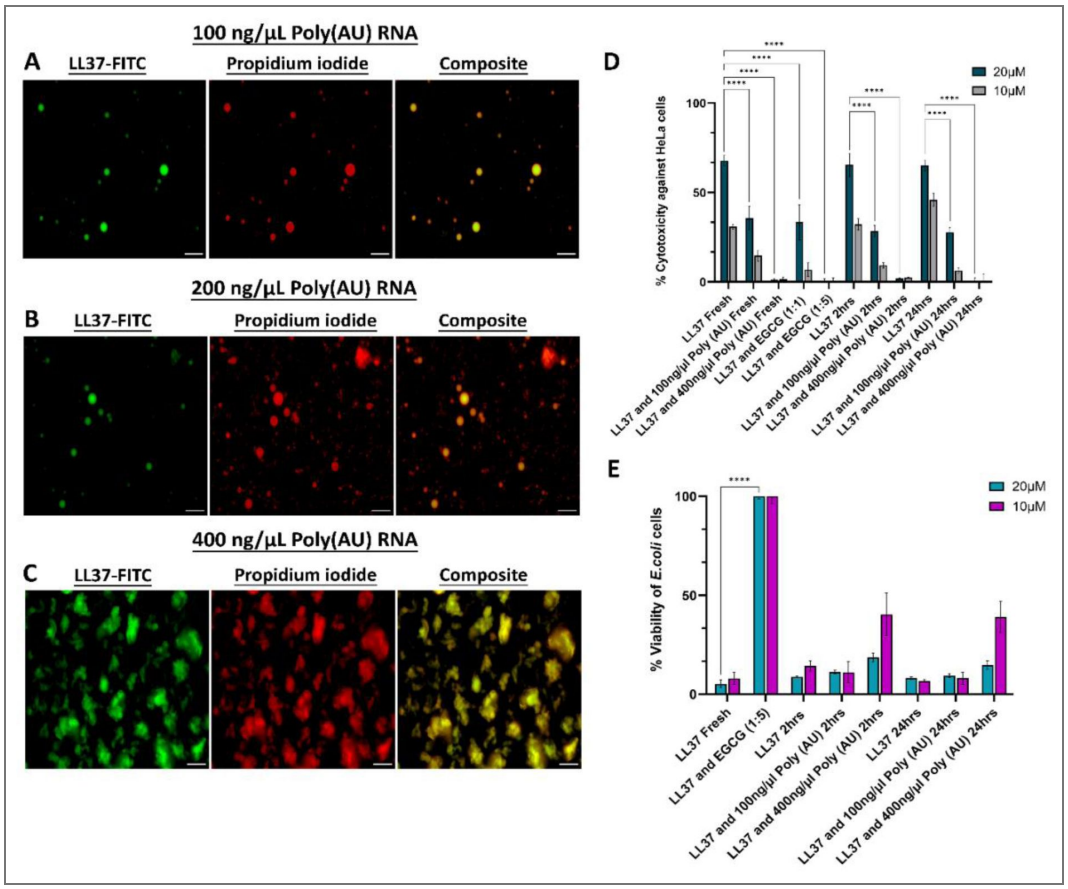

Figure 8. Effect of RNA concentration on LL-37 phase separation, aggregation, and activity at pH 7 after heat shock.

Fluorescence microscopy images showing 20% FITC-labelled (green) and 80% unlabelled 100 µM LL-37 in the presence of increasing concentrations: 100 ng/µL (**A**), 200 ng/µL (**B**) and 400 ng/µL (**C**) of Poly (AU) RNA (PI-labelled, red) after heat shock at 65°C for 15 minutes at pH 7. Scale bars represent 20 µm. **(D)** LL-37 cytotoxicity, with and without Poly (AU) RNA and EGCG at varying concentrations, was assessed in HeLa cells using the LDH colorimetric assay. The experiment was performed in triplicate and repeated on three separate days for reproducibility. Cytotoxicity percentages represent the average of all replicates, with error bars indicating the standard error of the mean. **(E)** The antimicrobial activity of LL-37, with and without Poly (AU) RNA and EGCG at varying concentrations, was evaluated against *E. coli* using the PrestoBlue Cell Viability assay. The experiment was performed in triplicate and repeated on three separate days for reproducibility. Bacterial viability percentages represent the average of all replicates, with error bars indicating the standard error of the mean. Statistical significance (**D-E**): *p < 0.05, **p < 0.01, ***p < 0.001, ****p < 0.0001 (one-way ANOVA, GraphPad Prism v11).

cytotoxic activity, mutants that retain α-helical monomeric structure yet fail to fibrillate lose toxicity[14,15], and fully matured fibrils are largely inactive[84,85]. This apparent paradox is resolved by proposing that the toxic window resides within dynamic, membrane-associated assembly intermediates[52]. In this framework, membrane-associated fibril growth may destabilize bilayers through lipid recruitment and extraction[86], analogous to mechanisms proposed for certain human amyloids such as islet amyloid polypeptide[87].

RNA preserves PSMα3 bioactivity by regulating this toxic window and redirecting its assembly pathway

In the absence of RNA, PSMα3 undergoes time-dependent aggregation[31], accompanied by progressive loss of cytotoxic and antimicrobial activity (Fig. 4), coinciding with the formation of dense, fibrillar assemblies (Figs. 2-3). These mature aggregates likely represent inert end states that sequester membrane-active intermediates[84,85]. RNA reshapes this trajectory in a concentration-dependent manner. At low RNA concentrations, PSMα3 initially retains activity (Fig. 4B) but gradually loses it as liquid-like RNA–PSMα3 condensates mature into more rigid assemblies (Figs. 2-4 & S3), indicating that RNA regulates the lifetime of dynamic intermediates. At higher RNA concentrations, RNA promotes alternative fibrillar polymorphs that retain substantial cytotoxic activity even after prolonged incubation (Fig. 4B). Similarly, RNA preserves antibacterial potency over time (Fig. 4A), consistent with stabilization of assembly states that remain competent for membrane interaction. Thus, RNA does not simply suppress aggregation but modulates the reversibility and supramolecular architecture of α-helical assemblies (Fig. S7), thereby controlling the duration and accessibility of the toxic window.

The temporal differences between cytotoxicity (Fig. 4B) and antibacterial activity (Fig. 4A) may reflect distinct membrane environments, aggregation kinetics, or interactions with bacterial surfaces versus mammalian membranes. Nonetheless, in both contexts, activity correlates with assembly state rather than peptide abundance alone. RNA therefore acts as a structural modulator that controls the lifetime and reversibility of functionally relevant intermediates.

Regulatory modulation versus irreversible inhibition

The contrasting effects of RNA and the amyloid inhibitor EGCG highlight that bioactivity is governed by supramolecular architecture and reversibility rather than aggregation per se. RNA preserves PSMα3 bioactivity by stabilizing dynamic, α-helical assembly states. In contrast, EGCG binds soluble PSMα3 and diverts it into stable amorphous aggregates that represent structural dead ends, abolishing activity (Figs. 6-7). Thus, EGCG should not be viewed as evidence that amyloid fibrils are the toxic species; instead, it abolishes activity by removing/redirecting soluble bioactive species into non-productive amorphous assemblies. Overall, RNA functions as a regulatory modulator of assembly dynamics, whereas EGCG enforces irreversible pathway diversion. These results underscore that assembly state, not simply peptide presence, determines biological function.

LL-37: non-amyloid α-helical assemblies under RNA control

In contrast to PSMα3, LL-37 does not form canonical amyloid architectures. Although it can assemble into α-helical fibrillar structures[53,56], these lack the ordered cross-β or cross-α stacking characteristic of amyloids. Nevertheless, RNA strongly modulates LL-37 behaviour. RNA can selectively attenuate cytotoxicity while preserving antimicrobial function, correlating with the formation of amorphous RNA–LL-37 co-assemblies rather than structured fibrils (Figs. 8, S11 & S15). RNA-dependent condensate-like assemblies are observed only under thermal stress, and these rapidly adopt solid-like properties (Figs. 8 and S12). For LL-37, RNA therefore appears to serve a protective role, minimizing collateral host damage while maintaining immune defence. This suggests that RNA-mediated modulation is a broader principle of α-helical peptide regulation, yet with a functional divergence that may reflect differences in the architecture of the resulting co-assemblies: RNA drives PSMα3 into structured α-helical fibrillar polymorphs, and LL-37 into disordered, amorphous co-aggregates.

Interestingly, although LL-37 does not adopt canonical amyloid architectures, it displays multiple functional connections to amyloid systems. LL-37 has been reported to bind the Alzheimer's-associated amyloid-β (Aβ) peptide and inhibit its fibrillization, likely through stabilization of prefibrillar intermediates[88]. This observation suggests that LL-37 can influence amyloid assembly pathways rather than simply interacting with mature fibrils, with potential implications for aging, immune regulation, and infection. In addition, LL-37 has been shown to interact with human α-synuclein as well as with bacterial curli amyloids, where it modulates biofilm properties[89–91]. Together, these findings position LL-37 as a cross-reactive regulator of amyloid assemblies across host and microbial contexts. The mechanistic basis and physiological relevance of these interactions remain to be further elucidated.

Parallels with phase-transition biology

The dynamic phase transitions observed for PSMα3 mirror those described for human RNA-binding proteins such as FUS, TDP-43, hnRNPA1, and tau, where LLPS enables physiological function but aberrant maturation contributes to neurodegenerative diseases[73,74,92–103].

Antimicrobial peptides can also induce LLPS with nucleic acids and disrupt critical processes like transcription and translation[104]. While the antimicrobial LL-37 is not an amyloid, its RNA-dependent co-assembly behaviour reinforces the broader concept that nucleic acids can regulate peptide phase behaviour across structurally distinct systems.

The nucleolar accumulation of PSMα3 (Fig. 5) is consistent with its intrinsic nucleic acid – binding capacity and provides cellular continuity with the RNA-dependent assemblies observed in vitro (Figs. 2-3). However, given the rapid membrane disruption induced by PSMα3 at cytotoxic concentrations (Figs. 5-6 and Movies S1-S2), nucleolar localization is unlikely to represent a distinct intracellular toxic mechanism. Rather, it reflects binding competence within RNA-rich compartments following cellular entry. The slow and incomplete fluorescence recovery observed in FRAP measurements (Fig. S8) further supports a dynamic yet constrained exchange of PSMα3 within the nucleolus, indicative of interaction with endogenous nucleic acids rather than freely diffusing peptide. The biological relevance of this interaction, particularly at sub-cytotoxic concentrations where membrane disruption does not dominate, remains to be determined and warrants further investigation.

Biological and therapeutic implications

Collectively, these findings position RNA as an environmental regulator of α-helical peptide assemblies, tuning bioactivity by modulating supramolecular organization and reversibility. Nucleic acids are abundant in infection-relevant settings where PSMs operate, including biofilms (rich in extracellular DNA and RNA), abscesses, neutrophil extracellular traps, and damaged tissues that release host RNA. In such contexts, RNA could control the persistence and timing of membrane-active PSM species by shifting assemblies between condensate-like reservoirs and more inert aggregates, thereby modulating virulence without invoking an intracellular mechanism. The divergent outcomes of RNA-mediated modulation-preservation of PSMα3 virulence versus attenuation of LL-37 cytotoxicity thus reflect peptide-specific assembly architectures rather than a uniform effect: RNA sustains dynamic, membrane-competent assemblies for the amyloidogenic PSMα3 while driving the non-amyloidogenic LL-37 into inactive amorphous states, effectively tilting the host-pathogen balance toward bacterial advantage.

While Poly (AU) served here as a defined, reductionist probe of peptide–RNA interactions, multiple endogenous RNA pools are plausible physiological partners. Within *S. aureus* biofilms, extracellular RNA is an abundant matrix component that contributes structurally to biofilm organization, raising the possibility that it directly modulates PSM assembly and thereby impacts biofilm stability and virulence-factor availability[105,106]. At infection sites, host-derived extracellular RNA released from stressed or dying cells can function as a danger-associated molecular pattern (DAMP)[107,108] and may further shift the balance between PSMα3-driven

cytotoxicity and LL-37–mediated host protection within inflammatory milieus. Defining which endogenous RNA species, concentrations, and structural features govern these assembly-dependent effects in vivo is therefore an important next step.

For PSMα3, RNA-sensitive assembly dynamics may provide a means for *S. aureus* to tune virulence in response to local cues, supporting immune evasion, biofilm-associated persistence, and survival across diverse host environments. For LL-37, RNA-mediated attenuation of cytotoxicity without loss of antimicrobial function suggests a host-protective mechanism that helps balance pathogen control with limiting collateral tissue damage. More broadly, this work shifts the conceptual emphasis from amyloid formation as a static endpoint to environmentally regulated phase/assembly transitions and shows that RNA-mediated control extends beyond canonical amyloids to non-amyloid α-helical assemblies. These insights motivate therapeutic strategies aimed at reshaping assembly pathways and material states, rather than simply blocking aggregation.

Methods

Peptide and Poly (AU) RNA preparation

Unlabelled and C-terminal FITC-labelled PSMα3 and LL-37 (PSMα3-FITC and LL-37-FITC) (>98% purity) were purchased from GL Biochem (Shanghai) Ltd. Poly (AU) RNA was purchased from Sigma Aldrich. A stock solution of the peptides was prepared at a concentration of 1 mM in a mixture of 20% dimethyl sulfoxide (DMSO) and 80% ultra-pure water. For light microscopy experiments, we used a mixture of 20% FITC-labelled and 80% unlabelled PSMα3 or LL-37. The Poly (AU) RNA stock solution was prepared at a concentration of 2000 ng/µl in UPW, the stock solution was stored at −80 °C until further use. Labelled Poly (AU) RNA was prepared by introducing 0.02 mg/ml of PI dye to the Poly (AU) RNA stock solution. For the experiments, samples containing 100 µM PSMα3 or LL-37 with Poly (AU) RNA at 10, 50, 100, 200, or 400 ng/µl were prepared in 50 mM HEPES buffer with 150 mM sodium chloride (NaCl), adjusted to pH 7.4, or in 20 µM Tris, 20 µM Bis-Tris, and 20 µM sodium acetate adjusted to pH 4.

Cytotoxicity against HeLa cells tested using the lactate dehydrogenase (LDH) release assay

Human cervical carcinoma HeLa cells (ATCC® CCL-2™) were routinely cultured in Dulbecco's Modified Eagle's Medium - high glucose (DMEM) (Sigma, Israel) with L-glutamine and supplemented with penicillin (100 U/ml), streptomycin (0.1 mg/ml), and with 10% foetal calf serum (Sigma, Israel). The cells grown at 37°C and 5% CO2. One day before the experiment, cells were resuspended in growing medium (DMEM supplemented with 10% foetal calf serum) $1X10^5$ cells/ml. 50 µL of cell suspension were pipetted into a 96-well plate and grown over night. Thirty minutes before the experiment cells were washed and resuspended in 50 µL of DMEM medium supplemented with L-glutamine (100 U/mL), and with penicillin (100 U/mL), streptomycin (0.1 mg/mL), and with 0.5% heat-inactivated foetal calf serum (assay medium). For the cytotoxicity assay, 100 µM PSMα3 was incubated with or without EGCG at molar ratios of 1:1 or 1:5, or with Poly (AU) RNA at concentrations of 50 ng/µL or 400 ng/µL, for the designated incubation times. Similarly, 100 µM LL-37 was prepared under the same conditions, with or without EGCG at 1:1 or 1:5 molar ratios, or Poly (AU) RNA at 100 ng/µL or 400 ng/µL, following the specified incubation times.

Serial two-fold dilutions in assay medium were performed, and 50 µL of each dilution were pipetted into the three different 96-well with the cells. The plates were incubated for 30 min at 37°C and 5% CO2 and then cell lysis was quantified using the LDH release colorimetric assay according to the manufacturer's instructions, including all recommended controls (LDH; Cytotoxicity Detection Kit Plus, Roche Applied Science, Germany). Cell-free assay medium was measured as background. Cells subjected to the same experimental conditions apart from peptide addition were used as a control to account for spontaneous LDH release. Cells subjected to the same experimental conditions apart from peptide addition and treated with manufacturer-

supplied lysis buffer were used as a control to account for maximum LDH release. Absorbance at 490 and 690 nm was measured in a plate reader (FLUOstar Omega, BMG Labtech, Germany). Absorbance at 690 nm was subtracted from 490 nm readings to correct for background. The mean absorbance of triplicate samples and controls was calculated, followed by background subtraction. Data was obtained from at least three independent biological replicates, with the arithmetic mean used for averaging. Error bars represent the standard deviation (SD). Statistical analysis, including one-way ANOVA, was performed using GraphPad Prism 10.

Assessment of Bacterial Viability Using PrestoBlue™ HS Cell Viability Reagent

Escherichia coli (E. coli) cultures were grown overnight in Luria Broth (LB) medium at 37 °C with shaking at 220 rpm. PSMα3 and LL-37 stock solutions were prepared by dissolving the peptides at a concentration of 1 mM in a solvent mixture of 20% DMSO and 80% ultra-pure water. From these stock solutions, the following sample preparations were made:

For PSMα3: **(1)**100 μM PSMα3 **(2)**100 μM PSMα3 with 50 ng/μL Poly (AU) RNA **(3)** 100 μM PSMα3 with 400 ng/μL Poly (AU) RNA **(4)** 100 μM PSMα3 with 500 μM EGCG. For LL-37: **(1)**100 μM LL-37 **(2)**100 μM LL-37 with 100 ng/μL Poly (AU) RNA **(3)** 100 μM LL-37 with 400 ng/μL Poly (AU) RNA **(4)** 100 μM LL-37 with 500 μM EGCG.

All solutions were prepared in 50 mM HEPES buffer pH 7.4 containing 150 mM NaCl. Where applicable, samples were incubated for the specified durations of 2 hours or 24 hours.

On the day of the experiment, dilutions of the PSMα3 solutions to 20 μM and 10 μM were prepared in LB medium and dispensed into a sterile 96-well black flat-bottom plate (Greiner bio-one). *E. coli* cultures were diluted to an optical density (OD) of 0.2, and bacterial suspensions were added to the wells. The plate was incubated at 37 °C with shaking at 220 rpm for 1 hour to allow the reaction to proceed.

Following incubation, 10X PrestoBlue™ HS Cell Viability Reagent (Invitrogen) was added to the wells. Wells containing only LB medium served as negative controls, while wells containing only *E. coli* served as positive controls. Plates were sealed with a thermal seal film (EXCEL Scientific) and incubated in a plate reader (CLARIOstar). Bacterial viability was assessed using PrestoBlue fluorescence (excitation: 535–560 nm; emission: 590–615 nm) over time. Each condition was tested in triplicate across three independent experiments. Fluorescence values were averaged, and blank readings were subtracted. Antimicrobial activity was determined at the 2-hour time point, when fluorescence was highest in the positive control. Data were obtained from at least three independent biological replicates, with the arithmetic mean used for averaging. Error bars represent the standard deviation (SD). Statistical analysis, including one-way ANOVA, was performed using GraphPad Prism 10.

Transmission electron microscopy (TEM)

For TEM analysis, 4–5 μL of 100 μM PSMα3, with or without EGCG or Poly (AU) RNA at concentrations of 10 ng/μL, 50 ng/μL, and 400 ng/μL, as well as 100 μM LL-37, with or without Poly (AU) RNA at 100 ng/μL and 400 ng/μL, were directly applied onto glow-discharged 400-mesh copper grids (easiGlow; Pelco, Clovis, CA, USA) with a grid hole size of 42 μm, stabilized with Formvar/carbon (Ted Pella, Inc.). The grids were glow-discharged using a 15-mA current with a negative charge for 25 seconds. Samples were allowed to adhere to the grids for 45 seconds before being stained with a 1% uranyl acetate solution (Electron Microscopy Science, 22400-1) for 45 seconds. The samples were then examined using a ThermoFisher Scientific (FEI) Talos F200C transmission electron microscope, operating at 200 kV and equipped with a Ceta 16M CMOS camera, at the Ilse Katz Institute for Nanoscale Science and Technology, Ben Gurion University of the Negev, Israel.

Turbidity measurements

Turbidity measurements were performed using a FLUOstar Omega plate reader (BMG Labtech) set to a wavelength of 400 nm. For each sample, the protein concentration was maintained at 100 µM, while RNA concentrations were varied across the following levels: 10 ng/µl, 20 ng/µl, 50 ng/µl, 100 ng /µl, 200 ng/µl, and 400 ng/µl. The turbidity of the mixtures was monitored over several hours following resuspension. The maximum absorbance recorded within the first 30 minutes was used as an indicator of the dense phase volume. The experiments were conducted three times with similar observations.

Electrophoretic mobility shift assay (EMSA)

RNA molecules were synthesized by IDT, with oligoA modified by the IRDye 800CW fluorescent dye. Double-stranded RNA was prepared by annealing 10 µM oligoA-IRDye 800CW with 10 µM oligoU in an annealing buffer containing 10 mM Tris-HCl (pH 7.5), 50 mM NaCl, and 1 mM EDTA. The mixture was heated to 95°C for 5 minutes, followed by gradual cooling to 25°C at a rate of 2°C per minute. The final RNA concentration used in the binding reactions was 40 nM (~400ng/µL).

RNA-protein complexes were incubated at 37°C for 30 minutes before being resolved on a 2.5% agarose gel. Gel electrophoresis was performed in a 0.5× TBE buffer for 7 minutes. The complexes were visualized using a Li-Cor Odyssey FC imaging system in the 800 nm channel with a 30-second exposure. For the EMSA, binding reactions were carried out in a buffer composed of 20 mM HEPES (pH 7.9), 50 mM KCl, 1 mM Dithiothreitol (DTT), 0.1 mM Ethylenediaminetetraacetic acid (EDTA), 5% glycerol, and 0.05% nonyl phenoxypolyethoxylethanol (NP-40). PSMα3 was added to the reactions at final concentrations of 0, 40, 80, 160, and 320 µM. The experiments were conducted three times with similar observations.

Fluorescent microscopy imaging of peptides with RNA in vitro

Prior to imaging, 100 µM PSMα3 or LL-37 (containing 20% FITC-labelled and 80% unlabelled peptide) were combined with PI-labelled Poly (AU) RNA at different concentrations in 50 mM HEPES buffer pH 7.4 containing 150 mM NaCl. Sample were also tested after 65°C heat shock for 15 minutes. In addition, the PSMα3 and RNA mixture was also tested in a different buffer containing 20 µM Tris, 20 µM Bis-Tris, and 20 µM sodium acetate at pH 4 and were subjected to heat shock at 65°C for 15 minutes.

Following preparation, with or without heat shock, a 10 µL aliquot of each sample was transferred to a µ-Slide 8 Well ibidi chamber or to a clean 24 × 60 mm No. 1.5 glass slide for imaging. Fluorescence microscopy was performed using a Leica DMI8 inverted fluorescent microscope equipped with a 63× immersion oil objective (Numerical Aperture, NA = 1.4) at the Life Sciences and Engineering (LS&E) Infrastructure Center, Technion-Israel Institute of Technology, Haifa, Israel. Data were processed and analyzed using Fiji-ImageJ software. The experiment was conducted three times with similar observations.

Fluorescence recovery after photobleaching (FRAP) measurements

FRAP experiments were conducted using a Zeiss LSM 710 laser scanning confocal microscope equipped with a 63× Plan-Apochromat oil immersion objective, NA1.4, at the Life Sciences and Engineering (LS&E) Infrastructure Center, Technion-Israel Institute of Technology, Haifa, Israel. The experiments were performed on condensates from by 100 µM PSMα3 or LL-37 (containing 20% FITC-labelled and 80% unlabelled peptide) mixed with PI-labelled Poly (AU) RNA at various concentrations as indicated in the figures. Photobleaching was performed using 405 nm and 488 nm laser lines. The experiments were conducted three times with similar observations.

For FRAP analysis inside the nucleolus of HeLa cells, PSMα3 was added to the cells at a final concentration of 20 µM containing 20% FITC-labelled and 80% unlabelled peptide. The cells were incubated with the peptide for 20 minutes before conducting the experiment. Data was processed and analysed using ZEISS ZEN software and Fiji-ImageJ software. The experiments were conducted three times with similar observations.

Total internal reflection fluorescence (TIRF) microscopy

TIRF microscopy was performed using a ZEISS Elyra 7 Super-Resolution Microscope equipped with a 63× Apochromat alpha Plan-Apochromat Oil immersion DIC objective, NA1.46, at the Life Sciences and Engineering (LS&E) Infrastructure Center, Technion-Israel Institute of Technology, Haifa, Israel. Images were acquired using the pco.edge sCMOS cameras, and data were processed and analysed with ZEISS ZEN software to accurately represent the observed phenomena. The condensates and aggregates analysed were generated using 100 µM of 20% FITC-PSMα3 (green) and 80% unlabelled PSMα3 with either 50 ng/µL or 400 ng/µL Poly (AU) RNA. AmyTracker 630 (Ebba Biotech) was added at a 1:500 (peptide: AmyTracker) molar ratio to each sample. The experiments were conducted three times with similar observations.

Confocal microscopy visualization of PSMα3 interaction with HeLa cells

HeLa cells were pre-cultured one day before the experiment by preparing a suspension containing 350,000 cells/ml and plating 150 µl of this suspension into each well of a µ-Slide 8 well glass-bottom chamber. The cells were then incubated overnight under standard growth conditions (37°C, 5% CO2) to allow for adherence and growth. On the day of the experiment, the cells were washed three times with phosphate-buffered saline (PBS) to remove any residual media. Hoechst 33342 dye (10 mg/mL stock) was diluted 1:2000 in fresh cell media and added to the cells. The cells were incubated with Hoechst for 10 minutes at 37°C and 5% CO2. After incubation, cells were washed three times with PBS to remove Hoechst residuals. A working solution of PI was prepared by diluting a 1 mg/ml PI stock solution to a final concentration of 0.02 mg/ml in fresh cell growth media. Immediately prior to imaging, PSMα3 was added to the cells at a final concentration of 20 µM containing 20% FITC-labelled and 80% unlabelled peptide. The cells were then imaged using a Ti2-E microscope by Nikon with a CSU-W1 spinning disk confocal unit by Yokogawa, equipped with a 100X CFI SR HP Plan Apochromat Lambda S silicone immersion objective, NA1.35, at the Life Sciences and Engineering (LS&E) Infrastructure Center, Technion-Israel Institute of Technology, Haifa, Israel. Confocal movies and images were captured by Photometrics BSI sCMOS cameras to observe the interaction and localization of PSMα3 within the cells, focusing particularly on its colocalization with nucleic acids in the nucleolar region. The acquired images and movies were subsequently analysed using Imaris Image Analysis Software (Oxford Instruments). The experiments were conducted three times with similar observations.

Super resolution light microscopy visualization of PSMα3 interaction with *E. coli*

E. coli lptD4213 cells were a kind gift from Prof. Sima Yaron from the Technion – Israel Institute of Technology. An inoculum was pre-cultured in Luria-Bertani medium (LB) medium at 220 rpm and 37°C for 24 hours prior to the experiment. On the day of the experiment, the optical density (OD) of the culture was measured, and the cells were diluted to an OD of 0.4. The cells were then incubated with 20 µM of 20% FITC-PSMα3 (green) and 80% unlabelled PSMα3, with and without EGCG at 1:5 molar ratio, alongside a bacteria-only control. Samples were incubated for 30 minutes at 220 rpm and 37°C. Following incubation, the samples were centrifuged three times for 3 minutes at 1.5g, with the supernatant discarded and the pellet resuspended in 1X PBS after each spin. The resuspended cells were then stained with 50 µg/mL wheat germ agglutinin (WGA) CF633 for 30 minutes. After staining, the cells were washed three times by centrifugation with PBS to remove excess WGA. During the final wash, the cells were resuspended in 0.1 mg/mL PI solution.

Prior to imaging, the samples were loaded into an ibidi µ-Slide VI 0.4. Imaging was performed using a ZEISS Elyra 7 Super-Resolution Microscope equipped with a 63× Apochromat alpha Plan-Apochromat Oil immersion DIC objective, NA 1.4, and pco.edge sCMOS cameras. Lattice structured illumination images were acquired and processed using the ZEN black software at the Life Sciences and Engineering (LS&E) Infrastructure Center, Technion-Israel Institute of Technology, Haifa, Israel. The experiments were conducted three times with similar observations.

Thioflavin T fluorescence fibrillation kinetics assay

Thioflavin T (ThT) (Sigma Aldrich) is a widely used fluorescent dye for detecting and analyzing amyloid fibril formation kinetics. Fibrillation curves in the presence of ThT typically exhibit an initial lag phase followed by rapid fibril elongation. To accurately capture the fibrillation lag time, PSMα3 was pre-treated before the experiment. The peptide was dissolved in a 1:1 mixture of 1,1,1,3,3,3-Hexafluoroisopropanol (HFIP-Sigma Aldrich) and Trifluoroacetic acid (TFA-Sigma Aldrich) to a final concentration of 1 mg/mL, followed by bath sonication for 10 minutes at room temperature. The organic solvents were then evaporated using a mini-rotational vacuum concentrator (Christ, Germany) at 1,000 rpm for 2 hours at room temperature.

For the experiment, freshly prepared 100 µM PSMα3 peptides, with or without 500 µM Epigallocatechin gallate (EGCG) at a 1:5 molar ratio, were prepared in 50 mM HEPES buffer pH 7.4 containing 150 mM NaCl. ThT was prepared by diluting a stock solution in ultrapure double-distilled water (UPddw) and filtered before use to reach a final concentration of 200 µM Blank control solutions containing all components except for the peptide were prepared for each reaction.

The assay was conducted in black 96-well flat-bottom plates (Greiner Bio-One), which were sealed with a thermal seal film (EXCEL Scientific) to prevent evaporation. Samples were incubated in a plate reader (OMEGA) at 37°C, shaking at 500 rpm for 85 seconds before each reading cycle, for up to 1,000 cycles of 6 minutes each, totalling approximately 100 hours.

Fluorescence was measured in triplicate using an excitation wavelength of 438 ± 20 nm and an emission wavelength of 490 ± 20 nm. All values were averaged, background fluorescence was subtracted using blank controls, and the results were plotted over time. Standard error of the mean is shown as error bars. The entire experiment was independently repeated at least three times on different days to ensure reproducibility.

Solid-State Circular Dichroism Spectroscopy

Solid-state circular dichroism spectroscopy(ss-CD) was conducted with PSMa3 to assess their fibrillar secondary structure components in presence and absence of Poly (AU) RNA. For preparation of peptide and RNA samples, see Peptide and Poly (AU) preparation section. PSMa3 was prepared at a working concentration of 100 µM in 50 mM HEPES, pH 7.4, 150 mM NaCl at 0 ng/µL, 50 ng/µL or 400 ng/µL Poly (AU) RNA. The reaction mixes were incubated for 0 min, 2 h and 72 h at 37 °C in a non-shaking thermocycler. Following incubation, soluble reaction components were removed via dilution washing with 150 µL water and centrifugation at 12.500 rcf for 30 min. 20 µL of the sediment were resuspended in 180 µL water for a second washing centrifugation step at 12.500 rcf for 30 min. 180 µL of the supernatant were discarded and 18 µL of sediment applied to a *Chirascan Series fused silica disc* (AP/CSSD, Applied Photophysics) in three times 6 µL steps. After every sample application onto to the silica disc, all liquid was evaporated at 37 °C for 5–10 min until only an opaque film remained visible. For secondary structure determination of aggregated/fibrillar peptide components on the silica disc, the disc was inserted into a *Chirascan solid sample holder* (CS/SSH, Applied Photophysics) and the circular dichroism recorded in the far-UV (180–250 nm, step size 1 nm, time-per-point 1 s) using a CD spectropolarimeter (Applied Photophysics). To counteract sample anisotropy, CD spectra were recorded at least four different disc rotations and the results averaged. Prior to data analysis, silica disc and buffer/water backgrounds were subtracted from recorded sample spectra. Poly (AU) RNA-only background spectra showed complex and high amplitude signals that did not appear for samples in combination with peptides and were therefore not subtracted from sample spectra.

NMR experiments

To prepare the reference samples for NMR analysis, 0.521 mg of PSMα3 was dissolved in 180 µL of 20 mM MES (2-(N-morpholino)ethanesulfonic acid) buffer at pH 6.0, supplemented with 5% (v/v) deuterium oxide (D_2O). From this solution, 170 µL was transferred into a 3.0 mm NMR tube for spectral acquisition. In parallel, a 4 mM stock solution of EGCG was prepared in the same 20 mM

MES buffer (pH 6.0). From this, a working solution containing 0.5 mM EGCG in 20 mM MES with 5% (v/v) D_2O was prepared to match the buffer conditions of the peptide sample. A volume of 170 µL was then transferred into a separate 3.0 mm NMR tube for use as the EGCG reference.

All NMR experiments were recorded on a Bruker 700 MHz spectrometer equipped with a triple-resonance cryoprobe (Prodigy) and an AVANCE NEO console. One-dimensional (1D) ^{1}H-NMR spectra were acquired using the Bruker library pulse sequence zggpw5 for water suppression. The acquisition parameters were: acquisition time (AQ) = 1.90 s, spectral width (SW) = 12.31 ppm, recovery delay (D1) = 1.5 s, and 64 scans. All experiments were conducted at 35 °C, under which optimal spectral quality was obtained.

Two-dimensional (2D) ^{1}H–^{1}H TOCSY (Total Correlation Spectroscopy) spectra were collected using the Bruker pulse sequence dipsi2gpph19. Acquisition parameters were: t_2 = 2048 complex points (AQ_2 = 0.118 s), t_1 = 512 complex points (AQ_1 = 0.029 s), $SW_1 = SW_2$ = 12.31 ppm, with 64 scans and a mixing time (tmix) of 80 ms. Recovery delay (D1) was set to 1.5 s. 2D ^{1}H–^{1}H NOESY (Nuclear Overhauser Effect Spectroscopy) spectra were acquired using the noesyfpgpph19 pulse sequence, with acquisition parameters identical to those used for TOCSY. The mixing time was set to 300 ms. Total experimental time for the combined 2D TOCSY and NOESY experiments was approximately 30 hours. NMR data processing was carried out using TopSpin 4.5.0 (Bruker), and spectral assignments for the 2D TOCSY and NOESY spectra were performed using POKY software[68]. Signal integration was carried out using in-house scripts written in Scilab[69].

Data availability

The data is available at *https://zenodo.org/records/17116616* and upon request

Supplementary figures

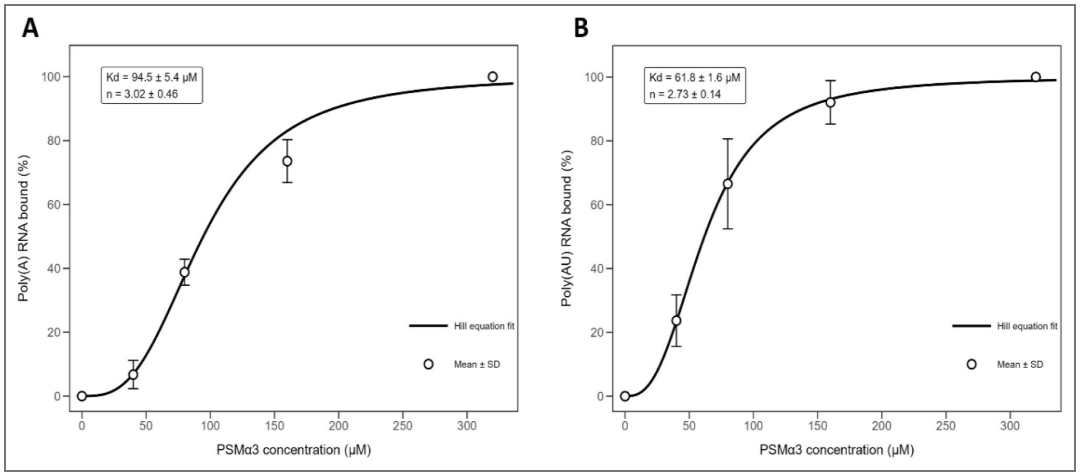

Figure S1. Concentration-dependent binding of PSMα3 to Poly (AU) and Poly (A) RNA. Percent RNA bound was quantified as a function of PSMα3 concentration for Poly AU) **(A)** and Poly(A) **(B)** calculated from the EMSA gels shown in Figure 1. Data points represent mean ± SD. Solid lines indicate fits to a Hill binding model with fixed asymptotes (0–100%). The apparent dissociation constant (Kd) corresponds to the protein concentration yielding 50% RNA binding, fitted Kd and Hill coefficient (n) values ± SE are shown.

Figure S2. Turbidity measurements of PSMα3 with increasing Poly (AU) RNA concentrations.

PSMα3 concentration was maintained at 100 μM, and Poly (AU) RNA concentrations varied across 0, 10, 20, 50, 100, 200, and 400 ng/μL. Data points represent the average optical density at 400 nm (OD400) recorded within the first 30 minutes post-resuspension, with each condition tested in triplicate. Error bars indicate the standard error of the mean.

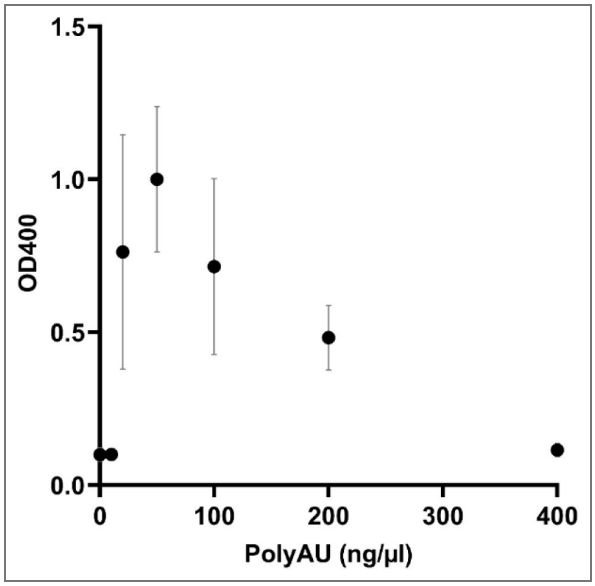

Figure S3. Encapsulation of Poly (AU) RNA within PSMα3-FITC droplets.

20% FITC-PSMα3 (green) and 80% unlabelled 100 μM PSMα3 were mixed with 50 ng/μL Poly (AU) RNA labelled with propidium iodide (PI). The left panel shows the FITC green channel, the middle panel displays the PI red channel, and the right panel is a composite image showing the overlap of PSMα3-FITC and Poly (AU) RNA-PI signals. Scale bars represent 20 μm.

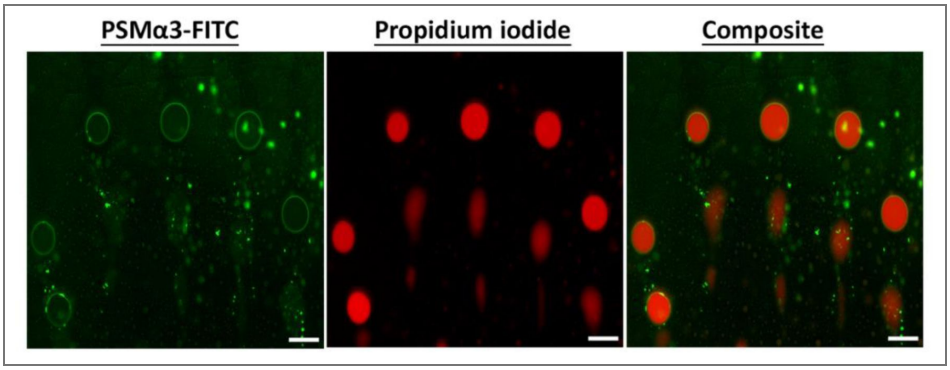

Figure S4. FRAP analysis of PSMα3 – Poly (AU) RNA condensate dynamics.

Normalized fluorescence recovery after photobleaching (FRAP) measured within condensates formed by 20% FITC-PSMα3 (green) and 80% unlabelled 100 μM PSMα3 in the presence of 50 ng/μL Poly (AU) RNA, corresponding to the experiment shown in Figure 2. Blue circles represent measured fluorescence intensity normalized to pre-bleach levels, and the red curve indicates a single-exponential fit to the recovery phase. The bleach event is marked by the orange arrow. Recovery reaches a plateau corresponding to a mobile fraction of 68% and an immobile fraction of 32%. The green marker and dashed line denote the half-time of recovery (t½ = 3.1 s). Horizontal dashed lines indicate pre-bleach intensity (top), plateau recovery level (middle), and immediate post-bleach intensity (bottom).

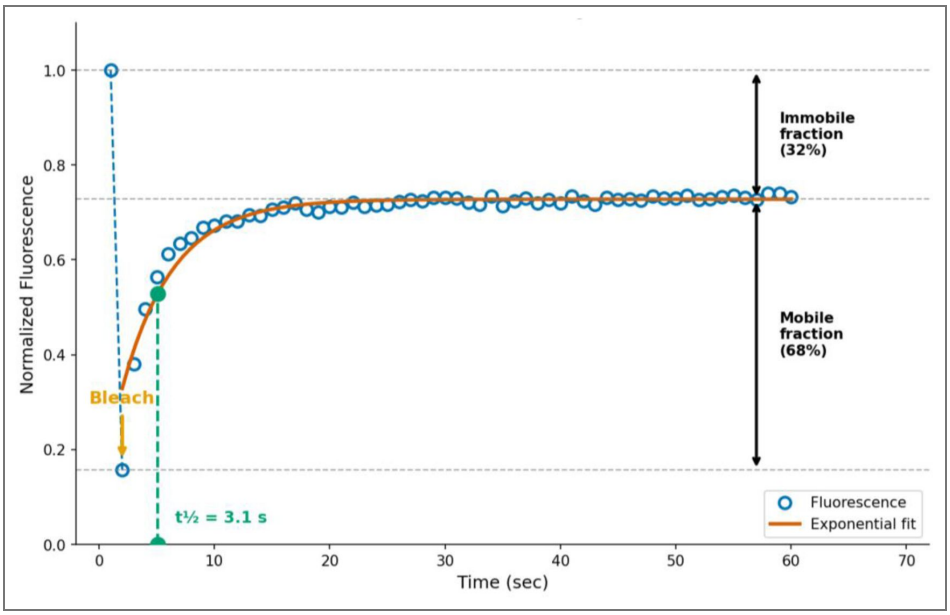

Figure S5. Colocalization analysis of PSMα3 and Poly (AU) RNA at different RNA concentrations.

Quantitative comparison of colocalization metrics for 100 μM PSMα3 (20% FITC-PSMα3 and 80% unlabelled) and Poly(AU) RNA at 50 ng/μL (blue) and 400 ng/μL (orange), corresponding to the experiment shown in Figure 2. Pearson's correlation coefficient was calculated using above-threshold pixels only, with thresholds determined automatically by the Costes method. Additional metrics include Spearman's rank correlation coefficient (ρ), Li's intensity correlation quotient (ICQ), and Manders' colocalization coefficients (tM1 and tM2) calculated using Costes automatic thresholding. Numeric values for each metric are indicated on the plot. The dashed vertical line at 0.5 marks a commonly used reference value for strong colocalization.

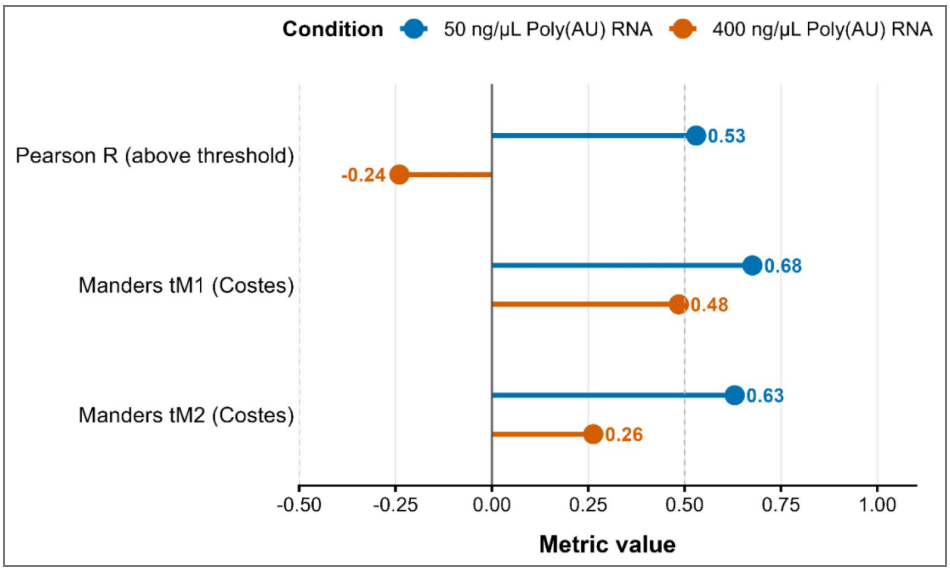

Figure S6. PSMα3 amyloid formation is enhanced by Poly (AU) RNA in a time- and concentration-dependent manner.

The graphs show the calculated AmyTracker (AT630) fluorescence intensity of 100 µM PSMα3 incubated with Poly (AU) RNA under the indicated conditions, corresponding to the experiment shown in Figure 3. Boxplots show the interquartile range with the centre line indicating the median; black diamonds denote the mean. Individual points represent independent measurements. Statistical significance was assessed using a Kruskal–Wallis test followed by Dunn's post hoc test with Bonferroni correction. *p < 0.05, **p < 0.01, ***p < 0.001, ****p < 0.0001.

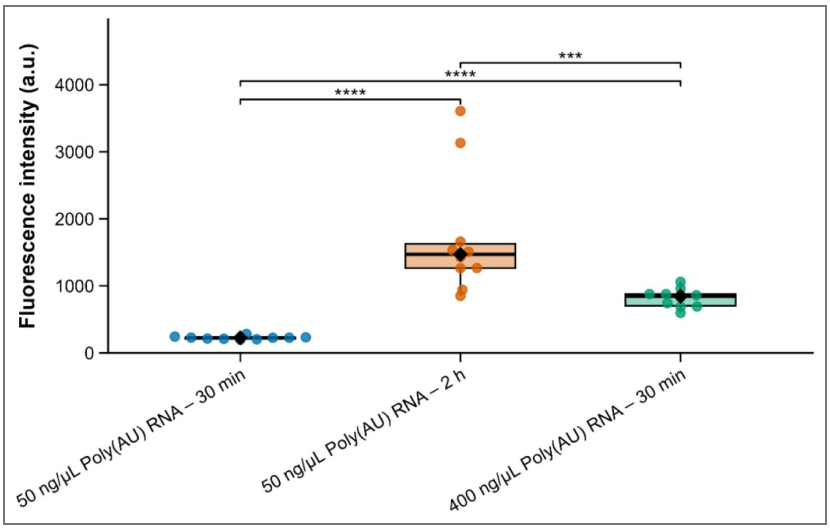

Figure S7. RNA stabilizes an α-helical conformation of PSMα3 over time.

Solid-state circular dichroism (ssCD) spectra of 100 µM PSMα3 incubated alone or with poly (AU) RNA at concentrations of 50 ng/µL and 400 ng/µL. Spectra were collected immediately after preparation (**A**), and after 2 hours of incubation (**B**). Measurements were recorded in the far-UV range (180–250 nm) to assess changes in secondary structure under the indicated conditions.

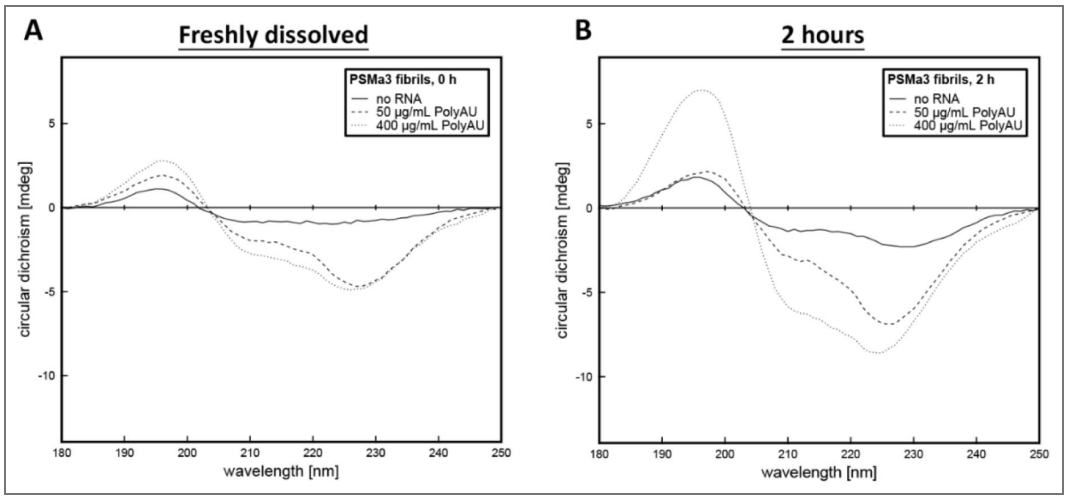

Figure S8. FRAP analysis of PSMα3 dynamics within the nucleolus of HeLa cells.

Normalized FRAP of 20% FITC-PSMα3 and 80% unlabelled 20 μM PSMα3 measured within the nucleolus of HeLa cells, corresponding to the experiment shown in Figure 5. Blue circles represent fluorescence intensity values normalized to the pre-bleach signal, and the orange line shows a single-exponential fit to the recovery kinetics. The photobleaching event is indicated by the orange arrow. Over the 60 s acquisition window, fluorescence recovery reached ~64%, corresponding to a mobile fraction of ~64% and an immobile fraction of ~36%. The recovery did not reach a clear plateau within the measured time frame, indicating the presence of a slowly exchanging or partially immobilized PSMα3 population within the nucleolus.

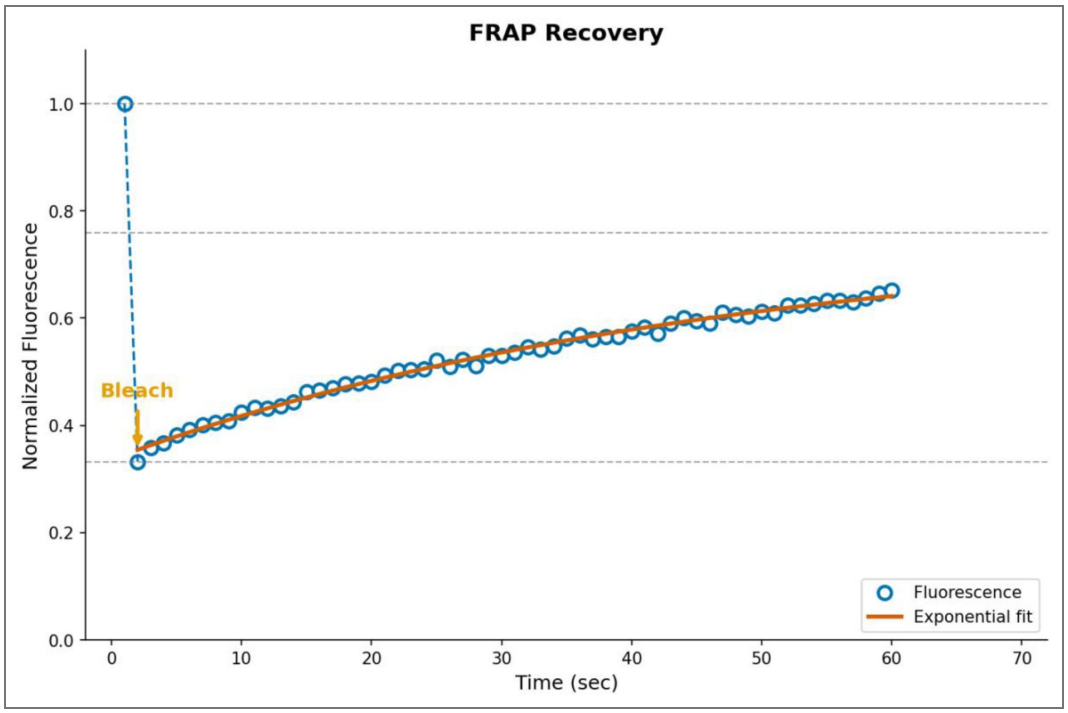

Figure S9. EGCG inhibits PSMα3 Fibrillation.

Fibrillation kinetics of 100 μM freshly dissolved PSMα3, monitored by Thioflavin-T (ThT) fluorescence. The data compares PSMα3 fibrillation in the absence (blue curve) and presence (red curve) of EGCG. The graph displays the mean fluorescence intensities from triplicate ThT measurements, with error bars representing the standard error of the mean.

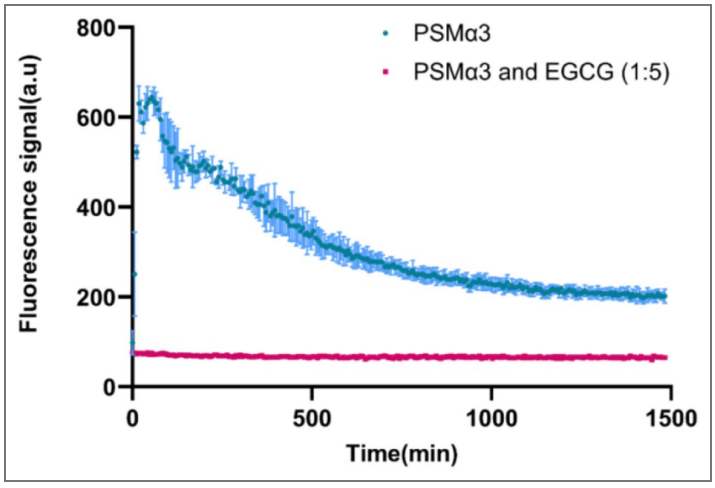

Figure S10. EGCG reduces the antimicrobial activity of PSMα3 against *E. coli*.

(A) Super-resolution light microscopy images of *E. coli* treated with 20 μM of 20% FITC-PSMα3 (green) and 80% unlabelled PSMα3 in the absence (left) and presence (right) of EGCG at a 1:5 molar ratio. Scale bars: 5 μm. **(B)** Antimicrobial activity of PSMα3 against *E. coli*, evaluated using the PrestoBlue cell viability assay, with and without EGCG (1:5 molar ratio). The experiments were performed in at least three replicates and repeated across three independent days to ensure result reliability. Cytotoxicity and bacterial cell viability percentages were calculated as the mean of all replicates, with error bars representing the standard error of the mean (SEM). Statistical significance was determined using one-way ANOVA for normally distributed data in GraphPad Prism (version 11). Significance levels are indicated as follows: *p<0.05, **p<0.01, ***p<0.001, ****p<0.0001.

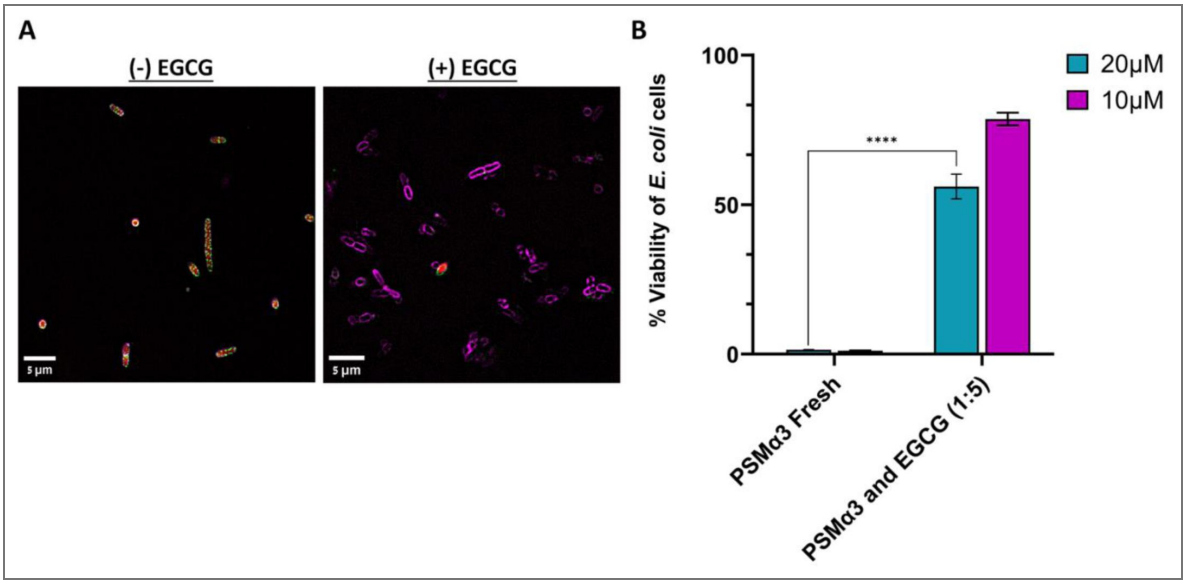

Figure S11. LL-37 undergoes aggregation with Poly (AU) RNA.

Light microscopy images showing 20% FITC-labelled (green) and 80% unlabelled 100 μM LL-37 (with no thermal stress) forming aggregates in the presence of 100 ng/μL Poly (AU) RNA, stained with PI (red). The composite image (right) highlights the colocalization of LL-37 and RNA (yellow), indicating RNA-induced aggregation. Scale bars: 20 μm.

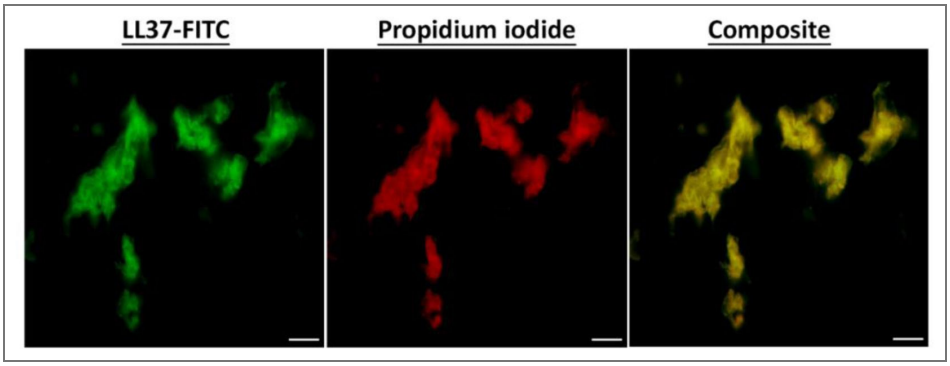

Figure S12. FRAP analysis of LL-37 – Poly (AU) RNA assemblies following heat shock.

(A) Representative fluorescence images of 20% FITC-labelled (green) and 80% unlabelled 100 μM LL-37 assemblies formed in the presence of 100 ng/μL Poly(AU) RNA in UB7 buffer, shown before photobleaching (Pre-Bleach), immediately after photobleaching (Bleach), and 60 s after bleaching (+60 Seconds). **(B)** Normalized FRAP corresponding to the bleached region shown in (A). Blue circles represent fluorescence intensity normalized to pre-bleach levels, and the orange curve shows a single-exponential fit to the recovery data. The bleach event is indicated by the orange arrow. Recovery reaches a low plateau corresponding to a mobile fraction of 10% and an immobile fraction of 90%. Horizontal dashed lines denote pre-bleach intensity (top), plateau recovery level (middle), and immediate post-bleach intensity (bottom).

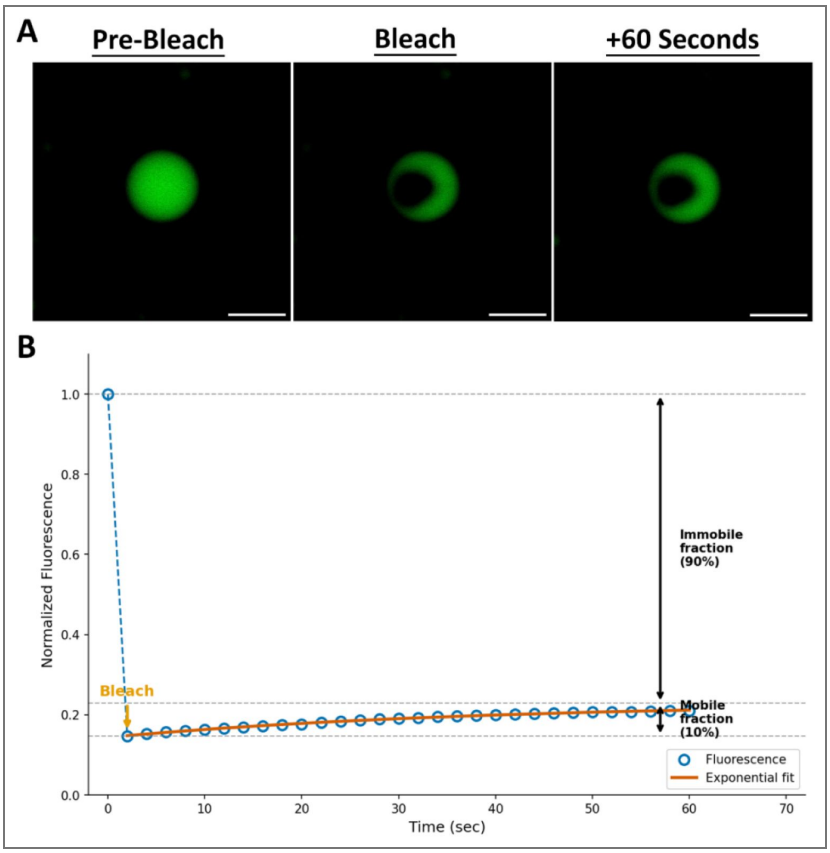

Figure S13. PSMα3 aggregates with Poly (AU) RNA after heat shock at physiological pH.

Light microscopy images showing 20% FITC-PSMα3 (green) and 80% unlabelled 100 μM PSMα3 forming aggregates with 50 ng/μL Poly (AU) RNA, stained with PI (red), after heat shock at 60°C for 15 minutes in 50 mM HEPES, 150 mM NaCl, at physiological pH (7.4). The composite image (right) highlights the colocalization of PSMα3 and RNA (yellow), indicating RNA-induced aggregation under heat stress. Scale bars: 20 μm.

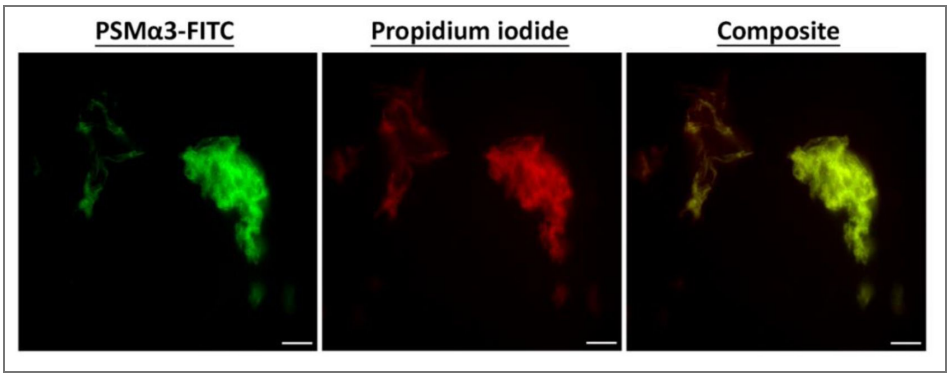

Figure S14. Effect of RNA concentration on PSMα3 phase separation and aggregation at pH 4 after heat shock.

Fluorescence microscopy images showing the effects on 20% FITC-PSMα3 (green) and 80% unlabelled 100 μM PSMα3 in the presence of increasing concentrations of Poly (AU) RNA (labelled with PI, red) following heat shock at 65°C for 15 minutes at pH 4. at 50 ng/μL (**A**), 100 ng/μL (**B**), 200 ng/μL (**C**) and 400 ng/μL (**D**). At a low RNA concentration of 50 ng/μL (**A**), clear phase separation of PSMα3 was observed, as evidenced by the presence of well-defined, spherical droplets. As the RNA concentration increased to 100 ng/μL, the droplets began to lose their spherical structure and showed more morphological irregularities (**B**). At RNA concentrations of 200 ng/μL and 400 ng/μL, a distinct transition to aggregation with irregular, amorphous clusters were observed (**C** and **D**, respectively). The composite images revealed an overlap between the PSMα3 and RNA, indicating co-localization during both phase separation and amorphous cluster formation. Scale bars in all images represent 20 μm.

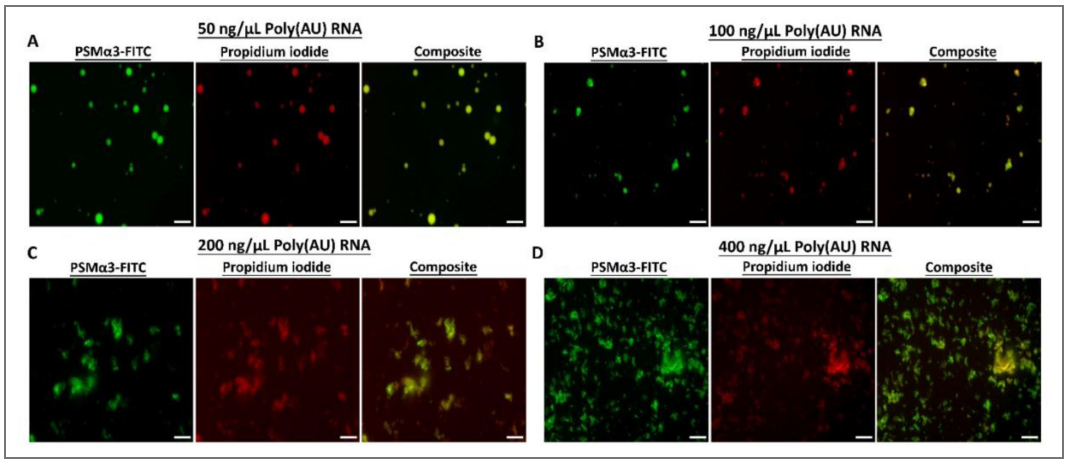

Figure S15. Poly (AU) RNA Modulates LL-37 Aggregation Dynamics Before and After Heat Shock.

TEM micrographs of 100 μM LL-37 incubated alone or with 100 ng/μL or 400 ng/μL Poly (AU) RNA for 2 hours or 24 hours. **(A)** Samples imaged before heat shock at the indicated point. **(B)** Samples subjected to a 65°C heat shock for 15 minutes, followed by further incubation for 2 or 24 hours before imaging.

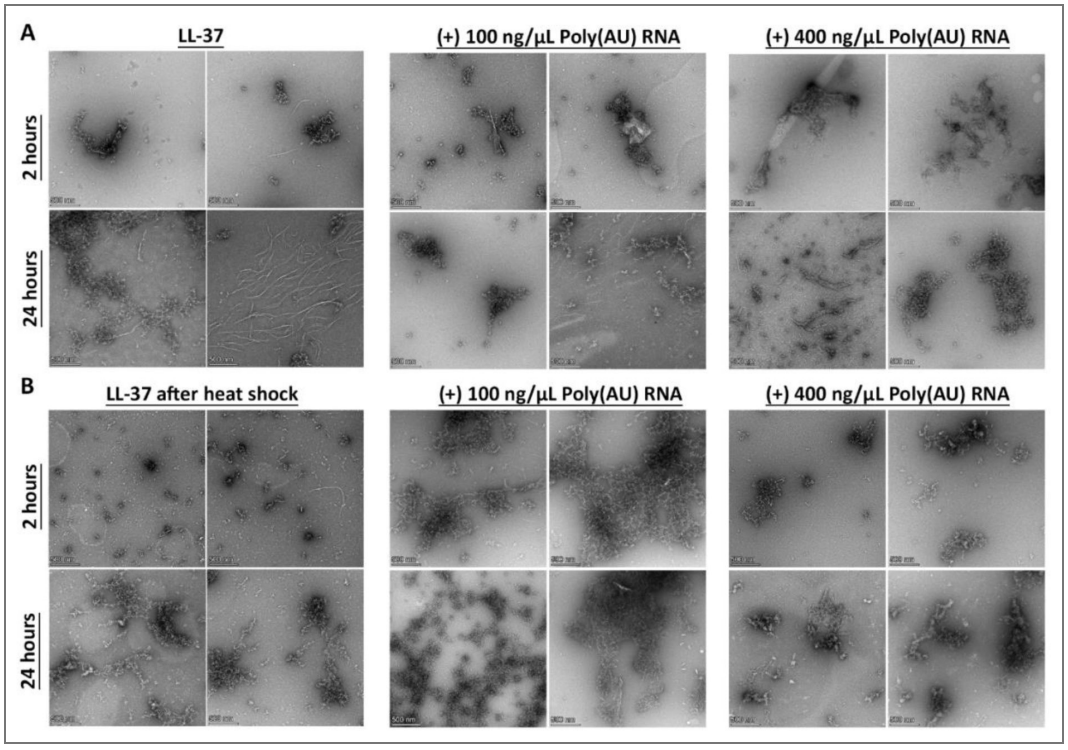

Acknowledgements

M.L. acknowledges research support from the Israel Science Foundation, Grant No. 2111/20 and the Cure Alzheimer's Fund. M.L. and M.Z. acknowledge the Forschungskooperation Niedersachsen – Israel, Volkswagenstiftung, No: 76251-4659/2022 (ZN 4042). Funded/Co-funded by the European Union (ERC, FuncAmyloid, 101087140). Views and opinions expressed are however those of the author(s) only and do not necessarily reflect those of the European Union or the European Research Council. Neither the European Union nor the granting authority can be held responsible for them. A.K.B thanks the Novo Nordisk Foundation (Grant number NNFSA17002839) and the European Union (ERC CoG 101088163 EMMA) for funding. We thank Ayala Shiber for advice and guidance, as well as Yael Mandel-Gutfreund and Hiba Hassanain for their assistance with RNA preparations. We acknowledge guidance and support from Nitsan Dahan from the Microscopy core facility center at the Lorry I. Lokey Interdisciplinary Center for Life Sciences and Engineering. We acknowledge the use of OpenAI's GPT-4 and other AI-based models to improve the writing quality of parts of this manuscript.

Additional files

Movie S1. Live-cell imaging of PSMα3-induced membrane permeabilization in HeLa cells. HeLa cells were incubated with 20 μM of 20% FITC-PSMα3 (green) and 80% unlabelled PSMα3 and monitored by time-lapse fluorescence microscopy. Nuclei were stained with Hoechst (blue). PI (red) was present in the imaging medium to detect loss of plasma membrane integrity. Time is shown in minutes: seconds (mm:ss) from peptide addition. Scale bar, 10 μm.

Movie S2. Live-cell imaging of EGCG-modulated PSMα3 activity in HeLa cells. HeLa cells were incubated with 20 μM of 20% FITC-PSMα3 (green) and 80% unlabelled PSMα3 in the presence of EGCG at a fivefold molar excess relative to PSMα3 (PSMα3: EGCG = 1:5) and monitored by time-lapse fluorescence microscopy. Nuclei were stained with Hoechst (blue). PI (red) was present in the imaging medium to detect loss of plasma membrane integrity. Time is shown in minutes:seconds (mm:ss) from peptide addition. Scale bar, 10 μm.

Additional information

Funding

Funder	Grant reference number	Author
Israel Science Foundation (ISF)	2111/20	Meytal Landau
Cure Alzheimer's Fund (CAF)		Meytal Landau
Forschungskooperation Niedersachsen - Israel, Volkswagenstiftung	76251-4659/2022 (ZN 4042)	Meytal Landau Markus Zweckstetter
EC | European Research Council (ERC)	https://doi.org/10.3030/101087140	Meytal Landau
Novo Nordisk Foundation	NNFSA17002839	Alexander Kai Buell
EC | European Research Council (ERC)	01088163	Alexander Kai Buell

Author ORCID iDs

Alexander K Buell: https://orcid.org/0000-0003-1161-3622
Meytal Landau: https://orcid.org/0000-0002-1743-3430

References

1. **Barnhart M. M.,** Chapman M. R (2006) Curli biogenesis and function. *Annu Rev Microbiol* **60**:131-147 https://doi.org/10.1146/annurev.micro.60.080805.142106 | PubMed

2. **Sleutel M.,** Pradhan B., Volkov A. N., Remaut H (2023) Structural analysis and architectural principles of the bacterial amyloid curli. *Nat Commun* **14**:2822 https://doi.org/10.1038/s41467-023-38204-2 | PubMed
3. **Howard M. K.,** et al. (2023) Probing the drivers of Staphylococcus aureus biofilm protein amyloidogenesis and disrupting biofilms with engineered protein disaggregases. *mBio* **14**:e00587-23 https://doi.org/10.1128/mbio.00587-23 | PubMed
4. **Salinas N.,** Povolotsky T. L., Landau M., Kolodkin-Gal I (2020) Emerging Roles of Functional Bacterial Amyloids in Gene Regulation, Toxicity, and Immunomodulation. *Microbiol Mol Biol Rev* **85**:e00062-20 https://doi.org/10.1128/mmbr.00062-20 | PubMed
5. **Van Gerven N.,** Van der Verren S. E., Reiter D. M., Remaut H (2018) The Role of Functional Amyloids in Bacterial Virulence. *J Mol Biol* **430**:3657-3684 https://doi.org/10.1016/j.jmb.2018.07.010 | PubMed
6. **Peña-Díaz S.,** Olsen W. P., Wang H., Otzen D. E (2024) Functional Amyloids: The Biomaterials of Tomorrow?. *Adv Mater* **36**:e2312823 https://doi.org/10.1002/adma.202312823 | PubMed
7. **Chapman M. R.,** et al. (2002) Role of Escherichia coli curli operons in directing amyloid fiber formation. *Science* **295**:851-855 https://doi.org/10.1126/science.1067484 | PubMed
8. **Blanco L. P.,** Evans M. L., Smith D. R., Badtke M. P., Chapman M. R (2012) Diversity, biogenesis and function of microbial amyloids. *Trends Microbiol* **20**:66-73 https://doi.org/10.1016/j.tim.2011.11.005 | PubMed
9. **Perov S.,** et al. (2019) Structural Insights into Curli CsgA Cross-β Fibril Architecture Inspire Repurposing of Anti-amyloid Compounds as Anti-biofilm Agents. *PLoS Pathog* **15**:e1007978 https://doi.org/10.1371/journal.ppat.1007978 | PubMed
10. **Golan N.,** et al. (2025) Resilience and charge-dependent fibrillation of functional amyloid: Interactions of Pseudomonas biofilm-associated FapB and FapC amyloids. *J Biol Chem* **301** https://doi.org/10.1016/j.jbc.2024.108096 | PubMed
11. **Jiang Y.,** et al. (2025) Natural Design of a Stabilized Cross-β Fold: Structure of the FuA FapC from Pseudomonas Sp. UK4 Reveals a Critical Role for Stacking of Imperfect Repeats. *Adv Mater* **37**:e2505503 https://doi.org/10.1002/adma.202505503 | PubMed
12. **Schwartz K.,** Syed A. K., Stephenson R. E., Rickard A. H., Boles B. R (2012) Functional amyloids composed of phenol soluble modulins stabilize Staphylococcus aureus biofilms. *PLoS Pathog* **8**:e1002744 https://doi.org/10.1371/journal.ppat.1002744 | PubMed
13. **Schwartz K.,** et al. (2014) The AgrD N-Terminal Leader Peptide of Staphylococcus aureus Has Cytolytic and Amyloidogenic Properties. *Infection and Immunity* **82**:3837-3844 https://doi.org/10.1128/iai.02111-14 | PubMed
14. **Tayeb-Fligelman E.,** Salinas N., Tabachnikov O., Landau M (2020) Staphylococcus aureus PSMα3 Cross-α Fibril Polymorphism and Determinants of Cytotoxicity. *Structure* **28**:301-313.e6 https://doi.org/10.1016/j.str.2019.12.006 | PubMed
15. **Tayeb-Fligelman E.,** et al. (2017) The cytotoxic Staphylococcus aureus PSMα3 reveals a cross-α amyloid-like fibril. *Science* **355**:831-833 https://doi.org/10.1126/science.aaf4901 | PubMed
16. **Kreutzberger M. A. B.,** et al. (2022) Phenol-soluble modulins PSMα3 and PSMβ2 form nanotubes that are cross-α amyloids. *Proc Natl Acad Sci U S A* **119**:e2121586119 https://doi.org/10.1073/pnas.2121586119 | PubMed
17. **Schwartz K.,** Boles B. R (2013) Microbial amyloids--functions and interactions within the host. *Curr Opin Microbiol* **16**:93-99 https://doi.org/10.1016/j.mib.2012.12.001 | PubMed
18. **Zhou X.,** et al. (2021) Staphylococcus aureus N-terminus formylated δ-toxin tends to form amyloid fibrils, while the deformylated δ-toxin tends to form functional oligomer complexes. *Virulence* **12**:1418-1437 https://doi.org/10.1080/21505594.2021.1928395 | PubMed
19. **Hansen K. H.,** et al. (2024) Structure of biofilm-forming functional amyloid PSMα1 from Staphylococcus aureus. *Proc Natl Acad Sci U S A* **121**:e2406775121 https://doi.org/10.1073/pnas.2406775121 | PubMed

20. **Wang X.,** et al. (2023) Staphylococcus aureus delta toxin modulates both extracellular membrane vesicle biogenesis and amyloid formation. *mBio* **14**:e0174823 https://doi.org/10.1128/mbio.01748-23 | PubMed
21. **Mehlin C.,** Headley C. M., Klebanoff S. J (1999) An Inflammatory Polypeptide Complex from Staphylococcus epidermidis: Isolation and Characterization. *J Exp Med* **189**:907-918 https://doi.org/10.1084/jem.189.6.907 | PubMed
22. **Chatterjee S. S.,** et al. (2013) Essential Staphylococcus aureus toxin export system. *Nat Med* **19**:364-367 https://doi.org/10.1038/nm.3047 | PubMed
23. **Kretschmer D.,** et al. (2010) Human formyl peptide receptor 2 senses highly pathogenic Staphylococcus aureus. *Cell Host Microbe* **7**:463-473 https://doi.org/10.1016/j.chom.2010.05.012 | PubMed
24. **Queck S. Y.,** et al. (2009) Mobile Genetic Element-Encoded Cytolysin Connects Virulence to Methicillin Resistance in MRSA. *PLoS Pathog* **5**:e1000533 https://doi.org/10.1371/journal.ppat.1000533 | PubMed
25. **Joo H.-S.,** Otto M (2012) Molecular basis of in vivo biofilm formation by bacterial pathogens. *Chem Biol* **19**:1503-1513 https://doi.org/10.1016/j.chembiol.2012.10.022 | PubMed
26. **Hu Z.,** et al. (2022) Phenol-soluble modulin α and β display divergent roles in mice with staphylococcal septic arthritis. *Commun Biol* **5**:1-11 https://doi.org/10.1038/s42003-022-03839-2 | PubMed
27. **Grando K.,** et al. (2022) Phenol-Soluble Modulins From Staphylococcus aureus Biofilms Form Complexes With DNA to Drive Autoimmunity. *Front Cell Infect Microbiol* **12** https://doi.org/10.3389/fcimb.2022.884065 | PubMed
28. **Cheung G. Y. C.,** Joo H.-S., Chatterjee S. S., Otto M (2014) Phenol-soluble modulins--critical determinants of staphylococcal virulence. *FEMS Microbiol Rev* **38**:698-719 https://doi.org/10.1111/1574-6976.12057 | PubMed
29. **Arad E.,** et al. (2023) Staphylococcus aureus functional amyloids catalyze degradation of β-lactam antibiotics. *Nat Commun* **14**:8198 https://doi.org/10.1038/s41467-023-43624-1 | PubMed
30. **Zaman M.,** Andreasen M (2020) Cross-talk between individual phenol-soluble modulins in Staphylococcus aureus biofilm enables rapid and efficient amyloid formation. *eLife* **9**:e59776 https://doi.org/10.7554/eLife.59776 | PubMed
31. **Rayan B.,** Barnea E., Khokhlov A., Upcher A., Landau M (2023) Differential fibril morphologies and thermostability determine functional roles of Staphylococcus aureus PSMα1 and PSMα3. *Front Mol Biosci* **10** https://doi.org/10.3389/fmolb.2023.1184785 | PubMed
32. **Marinelli P.,** Pallares I., Navarro S., Ventura S (2016) Dissecting the contribution of Staphylococcus aureus α-phenol-soluble modulins to biofilm amyloid structure. *Sci Rep* **6** https://doi.org/10.1038/srep34552 | PubMed
33. **Le K. Y.,** Dastgheyb S., Ho T. V., Otto M (2014) Molecular determinants of staphylococcal biofilm dispersal and structuring. *Front Cell Infect Microbiol* **4** https://doi.org/10.3389/fcimb.2014.00167 | PubMed
34. **Peschel A.,** Otto M. (2013) Phenol-soluble modulins and staphylococcal infection. *Nat Rev Microbiol* **11**:667-673 https://doi.org/10.1038/nrmicro3110 | PubMed
35. **Mehlin C.,** Headley C. M., Klebanoff S. J (1999) An Inflammatory Polypeptide Complex from Staphylococcus epidermidis: Isolation and Characterization. *J Exp Med* **189**:907-918 https://doi.org/10.1084/jem.189.6.907 | PubMed
36. **Chatterjee S. S.,** et al. (2013) Essential Staphylococcus aureus toxin export system. *Nat Med* **19**:364-367 https://doi.org/10.1038/nm.3047 | PubMed
37. **Seuring C.,** et al. (2020) The three-dimensional structure of human β-endorphin amyloid fibrils. *Nat Struct Mol Biol* **27**:1178-1184 https://doi.org/10.1038/s41594-020-00515-z | PubMed

38. **Banerjee P. R.,** Milin A. N., Moosa M. M., Onuchic P. L., Deniz A. A (2017) Reentrant Phase Transition Drives Dynamic Substructure Formation in Ribonucleoprotein Droplets. *Angew Chem Int Ed Engl* **56**:11354-11359 https://doi.org/10.1002/anie.201703191 | PubMed

39. **Morelli C.,** et al. (2024) RNA modulates hnRNPA1A amyloid formation mediated by biomolecular condensates. *Nat Chem* **16**:1052-1061 https://doi.org/10.1038/s41557-024-01467-3 | PubMed

40. **Cheung G. Y. C.,** et al. (2014) Insight into structure-function relationship in phenol-soluble modulins using an alanine screen of the phenol-soluble modulin (PSM) α3 peptide. *FASEB J* **28**:153-161 https://doi.org/10.1096/fj.13-232041 | PubMed

41. **Wang R.,** et al. (2007) Identification of novel cytolytic peptides as key virulence determinants for community-associated MRSA. *Nat Med* **13**:1510-1514 https://doi.org/10.1038/nm1656 | PubMed

42. **Laabei M.,** Jamieson W. D., Yang Y., van den Elsen J., Jenkins A. T. A. (2014) Investigating the lytic activity and structural properties of Staphylococcus aureus phenol soluble modulin (PSM) peptide toxins. *Biochim Biophys Acta* **1838**:3153-3161 https://doi.org/10.1016/j.bbamem.2014.08.026 | PubMed

43. **Ragonis-Bachar P.,** et al. (2022) Natural Antimicrobial Peptides Self-assemble as α/β Chameleon Amyloids. *Biomacromolecules* **23**:3713-3727 https://doi.org/10.1021/acs.biomac.2c00582 | PubMed

44. **Salinas N.,** et al. (2021) The amphibian antimicrobial peptide uperin 3.5 is a cross-α/cross-β chameleon functional amyloid. *Proc Natl Acad Sci U S A* **118**:e2014442118 https://doi.org/10.1073/pnas.2014442118 | PubMed

45. **Bücker R.,** et al. (2022) The Cryo-EM structures of two amphibian antimicrobial cross-β amyloid fibrils. *Nat Commun* **13**:4356 https://doi.org/10.1038/s41467-022-32039-z | PubMed

46. **Strati F.,** et al. (2025) Structural and Functional Versatility of the Amyloidogenic Non-Amidated Variant of the Antimicrobial Peptide Citropin 1.3. *Adv Sci (Weinh)* **12**:e03997 https://doi.org/10.1002/advs.202503997 | PubMed

47. **Landau M.,** et al. (2026) Expanding the amyloid landscape: structural plasticity of antimicrobial peptides. *Research Square* https://doi.org/10.21203/rs.3.rs-8249669/v1

48. **Tempra C.,** La Rosa C., Lolicato F (2021) The role of alpha-helix on the structure-targeting drug design of amyloidogenic proteins. *Chem Phys Lipids* **236** https://doi.org/10.1016/j.chemphyslip.2021.105061 | PubMed

49. **Ramamoorthy A.,** Lim M. H (2013) Structural characterization and inhibition of toxic amyloid-β oligomeric intermediates. *Biophys J* **105**:287-288 https://doi.org/10.1016/j.bpj.2013.05.004 | PubMed

50. **Ghosh D.,** et al. (2015) Structure based aggregation studies reveal the presence of helix-rich intermediate during α-Synuclein aggregation. *Sci Rep* **5**:9228 https://doi.org/10.1038/srep09228 | PubMed

51. **Salinas N.,** Colletier J.-P., Moshe A., Landau M (2018) Extreme amyloid polymorphism in Staphylococcus aureus virulent PSMα peptides. *Nat Commun* **9**:3512 https://doi.org/10.1038/s41467-018-05490-0 | PubMed

52. **Cali M. P.,** et al. (2026) The Many Lives of a Single Sequence: Functional Plasticity Through Amyloid Polymorphism. *Subcell Biochem* **113**:521-558 https://doi.org/10.1007/978-3-032-05273-5_16 | PubMed

53. **Sancho-Vaello E.,** et al. (2020) The structure of the antimicrobial human cathelicidin LL-37 shows oligomerization and channel formation in the presence of membrane mimics. *Sci Rep* **10** https://doi.org/10.1038/s41598-020-74401-5 | PubMed

54. **Zeth K.,** Sancho-Vaello E (2021) Structural Plasticity of LL-37 Indicates Elaborate Functional Adaptation Mechanisms to Bacterial Target Structures. *Int J Mol Sci* **22**:5200 https://doi.org/10.3390/ijms22105200 | PubMed

55. **Porcelli F.,** et al. (2008) NMR structure of the cathelicidin-derived human antimicrobial peptide LL-37 in dodecylphosphocholine micelles. *Biochemistry* **47**:5565-5572 https://doi.org/10.1021/bi702036s | PubMed

56. **Engelberg Y.,** Landau M (2020) The Human LL-37(17-29) antimicrobial peptide reveals a functional supramolecular structure. *Nat Commun* **11**:3894 https://doi.org/10.1038/s41467-020-17736-x | PubMed

57. **Rumpret M.,** et al. (2021) Signal inhibitory receptor on leukocytes-1 recognizes bacterial and endogenous amphipathic α-helical peptides. *FASEB J* **35**:e21875 https://doi.org/10.1096/fj.202100812r | PubMed

58. **Golan N.,** Engelberg Y., Landau M (2022) Structural Mimicry in Microbial and Antimicrobial Amyloids. *Annual Review of Biochemistry* **91**:403-422 https://doi.org/10.1146/annurev-biochem-032620-105157 | PubMed

59. **Rautenberg M.,** Joo H.-S., Otto M., Peschel A (2011) Neutrophil responses to staphylococcal pathogens and commensals via the formyl peptide receptor 2 relates to phenol-soluble modulin release and virulence. *FASEB J* **25**:1254-1263 https://doi.org/10.1096/fj.10-175208 | PubMed

60. **Syed A. K.,** Reed T. J., Clark K. L., Boles B. R., Kahlenberg J. M (2015) Staphlyococcus aureus phenol-soluble modulins stimulate the release of proinflammatory cytokines from keratinocytes and are required for induction of skin inflammation. *Infect Immun* **83**:3428-3437 https://doi.org/10.1128/iai.00401-15 | PubMed

61. **Schreiner J.,** et al. (2013) Staphylococcus aureus phenol-soluble modulin peptides modulate dendritic cell functions and increase in vitro priming of regulatory T cells. *J Immunol* **190**:3417-3426 https://doi.org/10.4049/jimmunol.1202563 | PubMed

62. **Chu M.,** et al. (2018) Staphylococcus aureus Phenol-Soluble Modulins α1-α3 Act as Novel Toll-Like Receptor (TLR) 4 Antagonists to Inhibit HMGB1/TLR4/NF-κB Signaling Pathway. *Front Immunol* **9** https://doi.org/10.3389/fimmu.2018.00862 | PubMed

63. **Kretschmer D.,** Nikola N., Dürr M., Otto M., Peschel A (2012) The Virulence Regulator Agr Controls the Staphylococcal Capacity to Activate Human Neutrophils via the Formyl Peptide Receptor 2. *J Innate Immun* **4**:201-212 https://doi.org/10.1159/000332142 | PubMed

64. **Bröker B. M.,** Mrochen D., Péton V (2016) The T Cell Response to Staphylococcus aureus. *Pathogens* **5** https://doi.org/10.3390/pathogens5010031 | PubMed

65. **Ganguly D.,** et al. (2009) Self-RNA-antimicrobial peptide complexes activate human dendritic cells through TLR7 and TLR8. *J Exp Med* **206**:1983-1994 https://doi.org/10.1084/jem.20090480 | PubMed

66. **Lee E. Y.,** et al. (2017) Crystallinity of Double-Stranded RNA-Antimicrobial Peptide Complexes Modulates Toll-Like Receptor 3-Mediated Inflammation. *ACS Nano* **11**:12145-12155 https://doi.org/10.1021/acsnano.7b05234 | PubMed

67. **Tewary P.,** et al. (2013) β-Defensin 2 and 3 promote the uptake of self or CpG DNA, enhance IFN-α production by human plasmacytoid dendritic cells, and promote inflammation. *J Immunol* **191**:865-874 https://doi.org/10.4049/jimmunol.1201648 | PubMed

68. **Schmidt N. W.,** et al. (2015) Liquid-crystalline ordering of antimicrobial peptide-DNA complexes controls TLR9 activation. *Nat Mater* **14**:696-700 https://doi.org/10.1038/nmat4298 | PubMed

69. **Lee E. Y.,** et al. (2019) Helical antimicrobial peptides assemble into protofibril scaffolds that present ordered dsDNA to TLR9. *Nat Commun* **10**:1012 https://doi.org/10.1038/s41467-019-08868-w | PubMed

70. **Tursi S. A.,** et al. (2017) Bacterial amyloid curli acts as a carrier for DNA to elicit an autoimmune response via TLR2 and TLR9. *PLOS Pathogens* **13**:e1006315 https://doi.org/10.1371/journal.ppat.1006315 | PubMed

71. **Gallo P. M.,** et al. (2015) Amyloid-DNA Composites of Bacterial Biofilms Stimulate Autoimmunity. *Immunity* **42**:1171-1184 https://doi.org/10.1016/j.immuni.2015.06.002 | PubMed

72. **Alberti S.,** Gladfelter A., Mittag T (2019) Considerations and Challenges in Studying Liquid-Liquid Phase Separation and Biomolecular Condensates. *Cell* **176**:419-434 https://doi.org/10.1016/j.cell.2018.12.035 | PubMed

73. **Hyman AA,** Weber CA, Jülicher F (2014) Liquid-liquid phase separation in biology. *Annual review of cell and developmental biology* **30** https://doi.org/10.1146/annurev-cellbio-100913-013325 | PubMed

74. **Wang B.,** et al. (2021) Liquid-liquid phase separation in human health and diseases. *Signal transduction and targeted therapy* **6** https://doi.org/10.1038/s41392-021-00678-1 | PubMed

75. **Xu Z.,** Wang W., Cao Y., Xue B (2023) Liquid-liquid phase separation: Fundamental physical principles, biological implications, and applications in supramolecular materials engineering. *Supramolecular Materials* **2** https://doi.org/10.1016/j.supmat.2023.100049

76. **Indig R. Y.,** Landau M (2023) Designed inhibitors to reduce amyloid virulence and cytotoxicity and combat neurodegenerative and infectious diseases. *Current Opinion in Chemical Biology* **75** https://doi.org/10.1016/j.cbpa.2023.102318 | PubMed

77. **Fernandes L.,** Cardim-Pires T. R., Foguel D., Palhano F. L (2021) Green Tea Polyphenol Epigallocatechin-Gallate in Amyloid Aggregation and Neurodegenerative Diseases. *Front Neurosci* **15** https://doi.org/10.3389/fnins.2021.718188 | PubMed

78. **Andrich K.,** Bieschke J (2015) The Effect of (-)-Epigallo-catechin-(3)-gallate on Amyloidogenic Proteins Suggests a Common Mechanism. *Adv Exp Med Biol* **863**:139-161 https://doi.org/10.1007/978-3-319-18365-7_7 | PubMed

79. **Nott T. J.,** et al. (2015) Phase Transition of a Disordered Nuage Protein Generates Environmentally Responsive Membraneless Organelles. *Mol Cell* **57**:936-947 https://doi.org/10.1016/j.molcel.2015.01.013 | PubMed

80. **Amico T.,** et al. (2024) A scale-invariant log-normal droplet size distribution below the critical concentration for protein phase separation. *eLife* **13**:RP94214 https://doi.org/10.7554/eLife.94214 | PubMed

81. **Ray S.,** Buell A. K (2024) Emerging experimental methods to study the thermodynamics of biomolecular condensate formation. *J Chem Phys* **160** https://doi.org/10.1063/5.0190160 | PubMed

82. **Sternke-Hoffmann R.,** Peduzzo A., Bolakhrif N., Haas R., Buell A. K (2020) The Aggregation Conditions Define Whether EGCG is an Inhibitor or Enhancer of α-Synuclein Amyloid Fibril Formation. *Int J Mol Sci* **21**:1995 https://doi.org/10.3390/ijms21061995 | PubMed

83. **Riback J. A.,** et al. (2017) Stress-Triggered Phase Separation Is an Adaptive, Evolutionarily Tuned Response. *Cell* **168**:1028-1040.e19 https://doi.org/10.1016/j.cell.2017.02.027 | PubMed

84. **Zheng Y.,** Joo H.-S., Nair V., Le K. Y., Otto M (2018) Do amyloid structures formed by Staphylococcus aureus phenol-soluble modulins have a biological function?. *Int J Med Microbiol* **308**:675-682 https://doi.org/10.1016/j.ijmm.2017.08.010 | PubMed

85. **Yao Z.,** et al. (2019) Use of a Stereochemical Strategy To Probe the Mechanism of Phenol-Soluble Modulin α3 Toxicity. *J Am Chem Soc* **141**:7660-7664 https://doi.org/10.1021/jacs.9b00349 | PubMed

86. **Malishev R.,** et al. (2018) Reciprocal Interactions between Membrane Bilayers and S. aureus PSMα3 Cross-α Amyloid Fibrils Account for Species-Specific Cytotoxicity. *J Mol Biol* **430**:1431-1441 https://doi.org/10.1016/j.jmb.2018.03.022 | PubMed

87. **Sparr E.,** et al. (2004) Islet amyloid polypeptide-induced membrane leakage involves uptake of lipids by forming amyloid fibers. *FEBS Lett* **577**:117-120 https://doi.org/10.1016/j.febslet.2004.09.075 | PubMed

88. **De Lorenzi E.,** et al. (2017) Evidence that the Human Innate Immune Peptide LL-37 may be a Binding Partner of Amyloid-β and Inhibitor of Fibril Assembly. *J Alzheimers Dis* **59**:1213-1226 https://doi.org/10.3233/jad-170223 | PubMed

89. **Kai-Larsen Y.,** et al. (2010) Uropathogenic Escherichia coli Modulates Immune Responses and Its Curli Fimbriae Interact with the Antimicrobial Peptide LL-37. *PLOS Pathogens* **6**:e1001010 https://doi.org/10.1371/journal.ppat.1001010 | PubMed

90. **Santos J.,** Ventura S., Pallarès I (2023) LL-37 and CsgC exemplify the crosstalk between anti-amyloid, antimicrobial, and anti-biofilm protein activities. *Neural Regen Res* **18**:1027-1028 https://doi.org/10.4103/1673-5374.355757 | PubMed

91. **Santos J.,** et al. (2021) α-Helical peptidic scaffolds to target α-synuclein toxic species with nanomolar affinity. *Nat Commun* **12**:3752 https://doi.org/10.1038/s41467-021-24039-2 | PubMed

92. **Murakami T.,** et al. (2015) ALS/FTD Mutation-Induced Phase Transition of FUS Liquid Droplets and Reversible Hydrogels into Irreversible Hydrogels Impairs RNP Granule Function. *Neuron* **88**:678-690 https://doi.org/10.1016/j.neuron.2015.10.030 | PubMed

93. **Wang Y.-L.,** et al. (2023) Liquid-liquid phase separation in DNA double-strand breaks repair. *Cell Death Dis* **14**:1-10 https://doi.org/10.1038/s41419-023-06267-0 | PubMed

94. **Kanaan N. M.,** Hamel C., Grabinski T., Combs B (2020) Liquid-liquid phase separation induces pathogenic tau conformations in vitro. *Nat Commun* **11**:2809 https://doi.org/10.1038/s41467-020-16580-3 | PubMed

95. **Ambadipudi S.,** Biernat J., Riedel D., Mandelkow E., Zweckstetter M (2017) Liquid–liquid phase separation of the microtubule-binding repeats of the Alzheimer-related protein Tau. *Nat Commun* **8** https://doi.org/10.1038/s41467-017-00480-0 | PubMed

96. **Boyko S.,** Surewicz W. K (2022) Tau liquid-liquid phase separation in neurodegenerative diseases. *Trends Cell Biol* **32**:611-623 https://doi.org/10.1016/j.tcb.2022.01.011 | PubMed

97. **Wegmann S.,** et al. (2018) Tau protein liquid–liquid phase separation can initiate tau aggregation. *The EMBO Journal* https://doi.org/10.15252/embj.201798049 | PubMed

98. **Babinchak W. M.,** et al. (2019) The role of liquid–liquid phase separation in aggregation of the TDP-43 low-complexity domain. *Journal of Biological Chemistry* **294**:6306-6317 https://doi.org/10.1074/jbc.ra118.007222 | PubMed

99. **Mukherjee S.,** Poudyal M., Dave K., Kadu P., Maji S. K (2024) Protein misfolding and amyloid nucleation through liquid–liquid phase separation. *Chem. Soc. Rev* **53**:4976-5013 https://doi.org/10.1039/d3cs01065a | PubMed

100. **Ray S.,** et al. (2020) α-Synuclein aggregation nucleates through liquid-liquid phase separation. *Nat Chem* **12**:705-716 https://doi.org/10.1038/s41557-020-0465-9 | PubMed

101. **Patel A.,** et al. (2015) A Liquid-to-Solid Phase Transition of the ALS Protein FUS Accelerated by Disease Mutation. *Cell* **162**:1066-1077 https://doi.org/10.1016/j.cell.2015.07.047 | PubMed

102. **Röntgen A.,** et al. (2025) Aggregation of α-synuclein splice isoforms through a phase separation pathway. *Sci Adv* **11**:eadq5396 https://doi.org/10.1126/sciadv.adq5396 | PubMed

103. **Elbaum-Garfinkle S** (2019) Matter over mind: Liquid phase separation and neurodegeneration. *J Biol Chem* **294**:7160-7168 https://doi.org/10.1074/jbc.rev118.001188 | PubMed

104. **Sneideris T.,** et al. (2023) Targeting nucleic acid phase transitions as a mechanism of action for antimicrobial peptides. *Nat Commun* **14**:7170 https://doi.org/10.1038/s41467-023-42374-4 | PubMed

105. **Mugunthan S.,** et al. (2023) RNA is a key component of extracellular DNA networks in Pseudomonas aeruginosa biofilms. *Nat Commun* **14**:7772 https://doi.org/10.1038/s41467-023-43533-3 | PubMed

106. **Chiba A.,** et al. (2022) Staphylococcus aureus utilizes environmental RNA as a building material in specific polysaccharide-dependent biofilms. *NPJ Biofilms Microbiomes* **8** https://doi.org/10.1038/s41522-022-00278-z | PubMed

107. **Preissner K. T.,** Fischer S (2023) Functions and cellular signaling by ribosomal extracellular RNA (rexRNA): Facts and hypotheses on a non-typical DAMP. *Biochim Biophys Acta Mol Cell Res* **1870**:119408 https://doi.org/10.1016/j.bbamcr.2022.119408 | PubMed

108. **Preissner K. T.,** Fischer S., Deindl E (2020) Extracellular RNA as a Versatile DAMP and Alarm Signal That Influences Leukocyte Recruitment in Inflammation and Infection. *Front Cell Dev Biol* **8** https://doi.org/10.3389/fcell.2020.619221 | PubMed

Peer reviews

Reviewer #1 (Public review):

Summary:

The manuscript by Rayan et al. aims to elucidate the role of RNA as a context-dependent modulator of liquid-liquid phase separation (LLPS), aggregation, and bioactivity of the amyloidogenic peptides PSMα3 and LL-37, motivated by their structural and functional similarities.

Strengths:

The authors combine extensive biophysical characterization with cell-based assays to investigate how RNA differentially regulates peptide aggregation states and associated cytotoxic and antimicrobial functions.

Weaknesses:

While the study addresses an interesting and timely question with potentially broad implications for host-pathogen interactions and amyloid biology, some aspects of the experimental design and data analysis require further clarification and strengthening.

https://doi.org/10.7554/eLife.109290.2.sa2

Reviewer #2 (Public review):

In this paper, Rayan et al. report that RNA influences cytotoxic activity of the staphylococcal secreted peptide cytolysin PSMalpha3 versus human cells and E. coli by impacting its aggregation. The authors used sophisticated methods of structural analysis and describe the associated liquid-liquid phase separation. They also compare to the influence of RNA on aggregation and activity of LL-37, which shows differences to that on PSMalpha3.

That RNA impacts PSM cytotoxicity when co-incubated in vitro becomes clear. However, I have two major problems with this study:

(1) The premise, as stated in the introduction and elsewhere, that PSMalpha3 amyloids are biologically functional, is highly debatable and has never been conclusively substantiated. The property that matters most for the present study, cytotoxicity, is generally attributed to PSM monomers, not amyloids. The likely erroneous notion that PSM amyloids are the predominant cytotoxic form is derived from an earlier study by the authors that has described a specific amyloid structure of aggregated PSMalpha3. Other authors have later produced evidence that, quite unsurprisingly, indicated that aggregation into amyloids decreases, rather than increases, PSM cytotoxicity. Unfortunately, yet other groups have in the meantime published in-vitro studies on "functional amyloids" by PSMs without critically challenging the concept of PSM amyloid "functionality". Of note, the authors' own data in the present study that show strongly decreased cytotoxicity of PSMalpha3 after prolonged incubation are in agreement with monomer-associated cytotoxicity as they can be easily explained by the removal of biologically active monomers from the solution.

In their revision and in the rebuttal, the authors have further described their concept regarding what they call "functionality" of PSMalpha3 amyloids. They now admit that monomers are the active cytolytic form, like other researchers have stressed, whereas amyloids are not. This represents a considerable difference to earlier papers in which they ascribed functionality, i.e. cytolytic capacity, to PSMalpha3 amyloids, a claim that has raised considerable controversy. Now, they use the term "functional " to describe that PSMalpha3

amyloids, while not cytolytic, can be reversed to a cytolytic monomeric state, calling them a "dynamic reservoir". There is no evidence that such a reservoir is necessary for the cytolytic activity of the monomers to be established; also, there is no evidence that in a biological system, such an amyloid reservoir exists. To continue calling PSMalpha3 amyloids "functional" based on this - considerably changed - concept of the authors appears inappropriate, given the finally admitted absence of cytolytic activity of the PSM amyloids in addition to the continuing complete lack of evidence of any biological relevance of PSM amyloid formation.

(2) That RNA may interfere with PSM aggregation and influence activity is not very surprising, given that PSM attachment to nucleic acids - while not studied in as much detail as here - has been described. Importantly, it does not become clear whether this effect has biologically significant consequences beyond influencing, again not surprisingly, cytotoxicity in vitro. The authors do show in nice microscopic analyses that labeled PSMalpha3 attaches to nuclei when incubated with HeLa cells. However, given that the cells are killed rapidly by membrane perturbation by the applied PSM concentrations, it remains unclear and untested whether the attachment to nucleic acids in dying cells makes any contribution to PSM-induced cell death or has any other biological significance.

Overall, the findings can be explained in a much more straightforward way with the common concept of cytotoxicity being due to monomeric PSMs, and the impact of nucleic acids on cytotoxicity being due to lowering of the concentration of that active form by RNA attachment. Further limiting the significance of the findings, whether this interaction has any biological significance on the physiology or infectivity of the PSM producer remains largely unexplored.

Further remarks:

• Circumstantial evidence based on the "amyloid inhibitor", EGCG: The results with EGCG, which has been shown to have a moderate amyloid-reducing effect on PSMalpha 1 and PSMalpha4, should not be taken as evidence for amyloid-based cytotoxicity. While increased concentrations of EGCG reduced the cytotoxic effect of PSMalpha3, it is not convincingly shown that this is due to a lower concentration of amyloid vs. monomeric PSM.

• It is appreciated that the authors refrain from presenting the unsubstantiated concept of "functional" PSM amyloids in the discussion. However, wording in that direction must also be removed from other parts of the manuscript (e.g. "bioactive fibrillar polymorphs". "The formation of cross-alpha amyloids has been correlated with toxic activity", etc.), generally refraining from uncritically implying that amyloid formation underlies PSM biological activity, and rather discussing that the much more likely explanation of the findings is a lowering of cytolytically active, monomeric PSM concentration.

• Discussion: "PSM alpha3 interaction with nucleic acids within human cells ...supports a comparable mechanism...". Delete. Unsubstantiated.

• The authors should cite papers that have argued against their hypothesis and not only their own manuscripts.

https://doi.org/10.7554/eLife.109290.2.sa1

Author response:

The following is the authors' response to the original reviews.

> ***Public Reviews:***
>
> ***Reviewer #1 (Public review):***

> *Summary:*
>
> *The manuscript by Rayan et al. aims to elucidate the role of RNA as a context-dependent modulator of liquid-liquid phase separation (LLPS), aggregation, and bioactivity of the amyloidogenic peptides PSMα3 and LL-37, motivated by their structural and functional similarities.*
>
> *Strengths:*
>
> *The authors combine extensive biophysical characterization with cell-based assays to investigate how RNA differentially regulates peptide aggregation states and associated cytotoxic and antimicrobial functions.*
>
> *Weaknesses:*
>
> *While the study addresses an interesting and timely question with potentially broad implications for host-pathogen interactions and amyloid biology, several aspects of the experimental design and data analysis require further clarification and strengthening.*
>
> *Major Comments:*
>
> *(1) In Figure 1A, the author showed "stronger binding affinity" based on shifts at lower peptide concentrations, but no quantitative binding parameters (e.g., apparent Kd, fraction bound, or densitometric analysis) are presented. This claim would be better supported by including: (i) A binding curve with quantification of free vs bound RNA band intensities (ii) Replicates and error estimates (mean {plus minus} SD).*

We thank the reviewer for this suggestion. To quantitatively support the binding differences observed in Figure 1A, we have now performed densitometric analysis of the EMSA data and included the results in Figure S1. The analysis showed that the Kd for PSMα3 binding to polyAU and polyA RNA is in the same order of magnitude but lower for the polyAU, indicating a stronger binding. A description was added to the results in lines 137-145 of the revised version.

> *(2) The authors report droplet formation at low RNA (50 ng/μL) but protein aggregation at high RNA (400 ng/μL) through fluorescence microscopy. However, no intermediate RNA concentrations (e.g., 100-300 ng/μL) are tested or discussed, leaving a critical gap in understanding the full phase diagram and transition mechanisms.*

Our initial choice of 50 ng/μL (low RNA) and 400 ng/μL (high RNA) was guided by a broader RNA titration performed by turbidity measurements across 0, 10, 20, 50, 100, 200, and 400 ng/μL (Figure S2 in the revised version). In this screen, turbidity increased up to 50 ng/μL and then decreased dose-dependently from 100–400 ng/μL. We interpret this non-monotonic behavior as consistent with a transition from a droplet rich regime (maximal light scattering at intermediate dense-phase volume) toward conditions where assemblies become larger and/or more compact and sediment out of the optical path. This is described in lines 158-161 of the revised version.

Of note, additional intermediate RNA conditions (100 and 200 ng/μL) are included in Figure S14 (of the revised version). While these experiments were performed under the heat-shock perturbation, they nevertheless support the central point that RNA tunes assembly state across intermediate concentrations rather than producing a binary low/high outcome.

Importantly, we agree with the reviewer that a full phase diagram would be the most rigorous way to define the transition mechanism. However, establishing csat and constructing a complete phase diagram would require systematic measurements of dilute-phase concentrations (e.g., centrifugation/quantification or fluorescence calibration),

controlled ionic strength titrations, and time-resolved mapping, which is beyond the scope of the present study. We have therefore revised the text to avoid implying that we provide a complete phase diagram. Instead, we frame our results as a qualitative with multi-assay characterization showing that RNA concentration drives a shift from liquid-like condensates (at low RNA) toward solid-like assemblies (at high RNA), with an intermediate regime suggested by the turbidity transition and supported by additional imaging under stress. Finally, to address the "critical gap" concern directly, we add a sentence (lines 239-241) stating that: "Future work will be required to quantitatively define the phase boundaries and delineate the dominant mechanisms, such as sedimentation, dissolution, or coarsening/aging, across intermediate RNA concentrations".

> *(3) Additionally, the behaviour of PSMα3 in the absence of RNA under LLPS conditions is not shown. Without protein-only data, it is difficult to assess if droplets are RNA-induced or if protein has a weak baseline LLPS that RNA tunes. The saturation concentration (csat) for PSMα3 phase separation, either in the absence or presence of RNA, should be reported.*

In response to the reviewer's request, we have added Figure 2F, which shows PSMα3 alone in the absence of RNA under the same conditions. PSMα3 does not form droplets in this condition, indicating that condensate formation is RNA-dependent in the tested conditions. This is referred to in the text in lines 190-193 of the revised version. Please see our response about determining the csat in the response to the previous comment.

> *(4) For a convincing LLPS claim, it is important to show: Quantitative FRAP curves (mobile fraction and half-time of recovery) rather than only microscopy images and qualitative statements.*

We have included quantitative FRAP analysis in Figure S4 of the revised version, showing normalized recovery curves along with extracted mobile fractions and half-times of recovery ($t_1/_2$). These quantitative measurements support the dynamic nature of the PSMα3–RNA. This is referred to in the text in lines 179-184 of the revised version.

> *(5) The manuscript highly relies on fluorescence microscopy to show colocalization. However, the colocalization is presented in a qualitative manner only. The manuscript would benefit from the inclusion of quantitative metrics (e.g., Pearson's correlation coefficient, Manders' overlap coefficients, or intensity correlation analysis).*

In response, we have added quantitative colocalization analysis to the revised manuscript. Specifically, we now report Pearson's correlation coefficients and Manders' overlap coefficients for the dual-channel fluorescence microscopy datasets in Figure S5 of the revised version. These metrics provide an objective measure of co-distribution and complement the qualitative imaging.

The analysis supports that at low RNA concentrations (droplet/condensate conditions), PSMα3 and RNA show strong colocalization, consistent with RNA being incorporated within, or closely associated with, the peptide-rich phase. In contrast, at high RNA concentrations, where the assemblies are more solid-like/amyloid-positive, the quantitative coefficients decrease, consistent with reduced overlap and an apparent spatial demixing in which RNA becomes partially excluded from the peptide-rich structures. This is referred to in the text in lines 194-203 of the revised version.

> *(6) In Figures 3 B and 3C, the contrast between "no AT630 at 30 min, strong at 2 h" (50 ng/μL) and "strong at 30 min" (400 ng/μL) is compelling, but a simple quantification (e.g., mean fluorescence intensity per area) would greatly increase rigor.*

We have included quantitative analysis of AmyTracker630 fluorescence intensity in Figure S6 of the revised version, reporting the mean fluorescence intensity per area for the indicated

conditions and time points. This quantification supports the qualitative differences observed in Figures 3B and 3C. This is now referred to in the text in lines 233-236 of the revised version.

> *(7) In Figure S3 ssCD data, if possible, indicate whether the α-helical signal increases with RNA concentration or shows a non-linear dependence, which might link to the LLPS vs solid aggregate regimes.*

The ssCD spectra displayed in Figure S7 in the revised version (corresponding to Figure S3 in the original submission) show that the α-helical signature of PSMα3 is markedly enhanced in the presence of RNA compared to peptide alone, as evidenced by increased signal intensity, deeper minima, and more pronounced spectral features characteristic of α-helical structure. Importantly, this enhancement is more pronounced at 400 ng/μL Poly(AU) RNA than at 50 ng/μL, particularly after 2 hours of coincubation, indicating that RNA concentration influences the stabilization of α-helical assemblies. This is now more specifically detailed in the text in lines 258-263 of the revised version.

We note that solid-state CD does not allow direct quantitative deconvolution of secondary structure content (e.g., % helix) in the same manner as solution CD, due to sample anisotropy, scattering, and orientation effects inherent to dried or aggregated films. Consequently, our interpretation is qualitative rather than strictly quantitative. The ssCD data therefore suggest a non-linear dependence on RNA concentration, rather than a simple linear dose–response. This is also expected considering that phase transition, suggested by the other findings, is intrinsically non-linear.

> *(8) In Figure 5B, FRAP recovery in dying cells may reflect artifactual mobility rather than biological relevance. Additionally, the absence of quantification data limits interpretation; providing recovery curves would clarify relevance."*

We added quantitative FRAP analysis of the effect on PSMα3 within HeLa cells, shown in Figure S8 of the revised version. Compared to PSMα3 assemblies *in vitro*, nucleolar PSMα3 exhibits slower fluorescence recovery and a reduced mobile fraction. The nucleolus represents a highly crowded, RNA-rich cellular environment, which is expected to impose additional constraints on molecular mobility and likely contributes to the slower recovery kinetics observed in cells. This is now more specifically detailed in the text in lines 324-333 and discussed in lines 597-607 of the revised version.

> *(9) The narrative conflates cytotoxicity endpoints (membrane damage, PI staining, aggregates) with localization data (nucleolar foci), creating ambiguity about whether nucleolar targeting drives toxicity or is a consequence of cell death. Separating toxicity assessment from localization analysis, or clearly demonstrating that nucleolar accumulation precedes cytotoxicity, would resolve this ambiguity.*

We thank the reviewer for raising this important point. We agree that, in the current dataset, cytotoxicity readouts (membrane damage, PI staining, aggregate formation) and subcellular localization (nucleolar accumulation) are observed in close temporal proximity, which limits our ability to unambiguously assign causality. In the experiments presented here, PSMα3 was applied at concentrations known to induce rapid membrane disruption and cytotoxicity in HeLa cells. Under these conditions, PSMα3 accumulates on cellular membranes and penetrates into the cell and nucleus on very short timescales (seconds to minutes), likely preceding the temporal resolution accessible by standard live-cell fluorescence microscopy. As a result, nucleolar accumulation and cytotoxic endpoints are detected essentially concurrently, precluding a definitive determination of whether nucleolar association actively drives toxicity or occurs as a downstream consequence of membrane permeabilization and cell damage.

We therefore emphasize that, in this study, nucleolar localization is presented as a phenomenological observation consistent with RNA-rich compartment association, rather than as a demonstrated causal mechanism of cytotoxicity. We have revised the Discussion (lines 597-607) to clarify this distinction and to avoid implying that nucleolar targeting is the primary driver of cell death.

We agree that resolving this ambiguity would require systematic time-resolved and concentration-dependent experiments, including analysis at sub-toxic PSMα3 concentrations below the membrane-disruptive threshold, combined with orthogonal imaging approaches. Such experiments are planned for future work but are beyond the scope of the present study.

> *(10) In Figure 8, to strengthen the LLPS assignment for LL-37, additional evidence, such as FRAP analysis or observation of droplet fusion events, would be valuable. This is particularly relevant given that the heat shock conditions (65 °C for 15 minutes) could potentially induce partial denaturation or nonspecific coacervation.*

In response to this comment, we have added FRAP analysis of LL-37 assemblies in the revised manuscript (Figure S12), including representative images and corresponding fluorescence recovery curves. The FRAP measurements show minimal fluorescence recovery over the acquisition window, indicating that the LL-37–RNA assemblies formed under these conditions are largely immobile and solid-like, rather than liquid-like droplets. This is now referred to in the text in lines 458-462 of the revised version.

> ***Reviewer #2 (Public review):***
>
> *In this paper, Rayan et al. report that RNA influences cytotoxic activity of the staphylococcal secreted peptide cytolysin PSMalpha3 versus human cells and E. coli by impacting its aggregation. The authors used sophisticated methods of structural analysis and described the associated liquid-liquid phase separation. They also compare the influence of RNA on the aggregation and activity of LL-37, which shows differences from that on PSMalpha3.*
>
> *Strengths:*
>
> *That RNA impacts PSM cytotoxicity when co-incubated in vitro becomes clear.*
>
> *Weaknesses:*
>
> *I have two major and fundamental problems with this study:*
>
> *(1) The premise, as stated in the introduction and elsewhere, that PSMalpha3 amyloids are biologically functional, is highly debatable and has never been conclusively substantiated. The property that matters most for the present study, cytotoxicity, is generally attributed to PSM monomers, not amyloids. The likely erroneous notion that PSM amyloids are the predominant cytotoxic form is derived from an earlier study by the authors that has described a specific amyloid structure of aggregated PSMalpha3. Other authors have later produced evidence that, quite unsurprisingly, indicated that aggregation into amyloids decreases, rather than increases, PSM cytotoxicity. Unfortunately, yet other groups have, in the meantime, published in-vitro studies on "functional amyloids" by PSMs without critically challenging the concept of PSM amyloid "functionality". Of note, the authors' own data in the present study, which show strongly decreased cytotoxicity of PSMalpha3 after prolonged incubation, are in agreement with monomer-associated cytotoxicity as they can be easily explained by the removal of biologically active monomers from the solution.*

We thank the reviewer for this important critique and agree that direct cytotoxicity is most plausibly mediated by soluble PSM species, while extensive fibrillation generally reduces

toxicity by depleting these forms, a conclusion supported by our data and by other studies (e.g., Zheng et al 2018 and Yao et al 2019). We do not propose mature amyloid fibrils as the primary toxic entities. Rather, we use the term functional amyloid in a regulatory sense, consistent with other biological amyloids whose fibrillar states modulate activity (e.g., hormone storage amyloids or RNA-binding proteins).

In line with emerging findings, we interpret PSMα3 toxicity as arising from a dynamic assembly process rather than from a single static molecular species. We previously showed that PSMα3 forms cross-α fibrils that are thermodynamically and mechanically less stable than cross-β amyloids and readily disassemble upon heat stress, fully restoring cytotoxic activity (Rayan et al., 2023). This behavior contrasts with PSMα1, which forms highly stable cross-β fibrils that do not recover activity after heat shock, suggesting that the limited thermostability of PSMα3 is an evolved feature enabling reversible switching between inactive (stored) and active states.

Consistent with this view, both PSMα1 and PSMα3 are cytotoxic in their soluble states, yet mutants unable to fibrillate lose activity, indicating that fibrillation is required but not itself the toxic end state (Tayeb-Fligelman et al., 2017, 2020; Malishev et al., 2018). Our other studies further show that cytotoxicity toward human cells correlates with inherent or lipid-induced α-helical assemblies, rather than with inert β-sheet amyloids (RagonisBachar et al., 2022, 2026; Salinas 2020, Bücker 2022). Together, these findings support a model in which membrane-associated, dynamic α-helical assembly, which requires continuous exchange between soluble species and growing fibrils, drives membrane disruption, potentially through lipid recruitment or extraction, analogous to mechanisms proposed for human amyloids such as islet amyloid polypeptide (Sparr et al., 2004).

In the present study, we further show that RNA reshapes this dynamic landscape: while PSMα3 alone progressively loses activity upon incubation, co-incubation with RNA preserves cytotoxicity by stabilizing bioactive polymorphs and condensate-like states, whereas high RNA concentrations promote solid aggregation but nevertheless preserve activity. Thus, aggregation is neither inherently functional nor toxic, but context dependent and environmentally regulated. Taken together, our data support a model in which PSMα3 amyloids act as a dynamic reservoir, enabling *S. aureus* to tune virulence by reversibly shifting between dormant and active states in response to environmental cues such as heat or RNA.

This is now discussed in lines 56-76 and 523-553 of the revised version.

> *(2) That RNA may interfere with PSM aggregation and influence activity is not very surprising, given that PSM attachment to nucleic acids - while not studied in as much detail as here - has been described. Importantly, it does not become clear whether this effect has biologically significant consequences beyond influencing, again not surprisingly, cytotoxicity in vitro. The authors do show in nice microscopic analyses that labeled PSMalpha3 attaches to nuclei when incubated with HeLa cells. However, given that the cells are killed rapidly by membrane perturbation by the applied PSM concentrations, it remains unclear and untested whether the attachment to nucleic acids in dying cells makes any contribution to PSM-induced cell death or has any other biological significance.*

We thank the reviewer for this important point and agree that PSM–nucleic acid interactions are not unexpected and that our data do not support a direct intracellular role for RNA binding in mediating cytotoxicity. Accordingly, we do not propose nucleolar or nuclear association of PSMα3 as a causal mechanism of cell death. At the concentrations used, PSMα3 induces rapid membrane disruption, and nucleic acid association is observed along with membrane attachment, precluding conclusions about intracellular function. This limitation is now explicitly clarified in the revised manuscript. The biological significance of our findings

lies instead in extracellular and environmental contexts, where PSMα3 encounters abundant nucleic acids, such as RNA or DNA released from damaged host cells or present in biofilms as now addressed in lines 622631. Our data show that RNA modulates PSMα3 aggregation trajectories, shifting the balance between liquid-like condensates and solid aggregates, and thereby regulates the persistence and timing of cytotoxic activity. In this framework, RNA acts as a context dependent regulator of virulence, rather than as an intracellular cytotoxic cofactor, an aspect which would be studied in depth in future work. This is now addressed in the text in lines 597-607 of the revised version.

> ***Reviewer #3 (Public review):***
>
> *Summary:*
>
> *The manuscript by Rayan et al. aims to investigate the role of RNA in modulating both virulent amyloid and host-defense peptides, with the objective of understanding their self-assembly mechanisms, morphological features, and aggregation pathways.*
>
> *Strengths:*
>
> *The overall content is well-structured with a logical flow of ideas that effectively conveys the research objectives.*
>
> *Weaknesses:*
>
> *(1) Figure 2 displays representative FRAP images demonstrating fluorescence recovery within seconds. To gain a more comprehensive understanding of how recovery after photobleaching varies under different conditions, it is recommended to supplement these images with corresponding quantitative fluorescence recovery curves for analysis.*

In response to this comment, we have supplemented the representative FRAP images with quantitative fluorescence recovery curves, reporting normalized recovery kinetics for the indicated conditions. These data are now provided in Figure S4 of the revised manuscript, allowing direct comparison of recovery behavior across conditions (shown by microscopy in Figure 2). In addition, we have included quantitative FRAP analyses for the cellular imaging shown in Figure 5 (presented in Figure S8) and for LL-37 assemblies formed under heat-shock conditions (Figure S12). Together, these additions provide a quantitative framework for interpreting the FRAP results and strengthen the distinction between liquid-like and solid-like assembly states.

> *(2) Ostwald ripening typically leads to the shrinkage or even disappearance of smaller droplets, accompanied by the further growth of large droplets. However, the droplet size in Figure 2D decreases significantly after 2 h of incubation. This observation prompts the question, what is the driving force underlying RNA-regulated phase separation and phase transition?"*

We thank the reviewer for this observation. Across multiple samples, we consistently observe a coexistence of small droplets and larger aggregates, rather than systematic growth of larger droplets at the expense of smaller ones or a uniform decrease in droplet size. In addition, the timescales examined do not allow us to reliably assess whether diffusion-driven droplet coalescence is fast enough to draw firm conclusions about droplet size evolution. This is now addressed in the text in lines 181-184 of the revised version.

A decrease in droplet size over time is nevertheless observed in some instances and is more consistent with a time-dependent conversion of initially liquid-like condensates into more solid-like assemblies, which would reduce molecular mobility and suppress droplet coalescence. In parallel, progressive fibril formation may act as a sink for soluble peptide, leading to partial dissolution or shrinkage of less mature condensates. Together, these

observations are consistent with a non-equilibrium aging process, in which RNAregulated assemblies evolve from dynamic condensates toward more solid structures rather than following equilibrium Ostwald ripening.

> *(3) The manuscript aims to study the role of RNA in modulating PSMα3 aggregation by using solution-state NMR to obtain residue-specific structural information. The current NMR data, as described in the method and figure captions, were recorded in the absence of RNA. Whether RNA binding induces conformational changes of PSMα3, and how these changes alter the NMR spectra? Also, the sequential NOE walk between neighboring residues can be annotated on the spectrum for clarity.*

The solution-state NMR experiments were performed specifically to characterize the potential binding of EGCG to PSMα3. Due to the strong tendency of PSMα3 to undergo rapid aggregation and line broadening upon RNA addition, solution state NMR spectra in the presence of RNA could not be obtained at sufficient quality for residue-specific analysis. As suggested, we have updated and annotated the sequential NOE walk between neighboring residues on the relevant NOESY spectra to improve clarity.

> *(4) The authors claim that LL-37 shares functional, sequence, and structural similarities with PSMα3. However, no droplet formation was observed of LL-37 in the presence of RNA only. The authors then applied thermal stress to induce phase separation of LL-37. What are the main factors contributing to the different phase behaviors exhibited by LL37 and PSMα3? What are the differences in the conformation of amyloid aggregates and the kinetics of aggregation between the condensation-induced aggregation in the presence of RNA and the conventional nucleation-elongation process in the absence of RNA for these two proteins?*

We appreciate this important question and have clarified both the basis of the comparison and the origin of the divergent phase behaviors of LL-37 and PSMα3. While PSMα3 and LL-37 share key properties as short, cationic, amphipathic α-helical peptides that self-assemble and interact with nucleic acids, they differ fundamentally in their assembly architectures. PSMα3 is an amyloidogenic peptide that forms cross-α amyloid fibrils, in which α-helices stack perpendicular to the fibril axis. In contrast, LL-37 can form fibrillar or sheet-like assemblies (observed in cryo grids), but these lack canonical amyloid features without clear cross-α or cross-β amyloid order, as so far observed by crystal structures. This is now clarified in different parts of the text of the revised version. Thus, the comparison between the two peptides is functional and physicochemical rather than implying identical amyloid mechanisms. These structural differences likely underlie their distinct phase behaviors.

Because LL-37 does not follow a classical amyloid nucleation–elongation pathway, and high-resolution structural information (e.g., cryo-EM) is currently lacking, partly due to its sheet-like, non-twisted morphology (unpublished results), it is not possible to directly compare aggregation kinetics or nucleation mechanisms between LL-37 and PSMα3. It is possible that amyloidogenic systems such as PSMα3 exhibit greater flexibility in prefibrillar and fibrillar polymorphism, enabling RNA-regulated phase behavior, whereas non amyloid assemblies such as LL-37 are more prone to stress-induced solid aggregation. We note that this interpretation is necessarily tentative and does not imply a general rule, but rather reflects differences evident in the present system.

> ***Recommendations for the authors:***
>
> ***Reviewer #1 (Recommendations for the authors):***
>
> *Minor Comments:*
>
> *(1) In the abstract, replacing the word "overriding" with "counteracting" may provide a scientifically neutral tone.*

In the course of revision, the abstract was substantially rewritten to more precisely convey the mechanistic framework and key conclusions of the study. As part of this rewrite, the term "overriding" was removed and the language throughout was revised to adopt a more scientifically neutral tone, consistent with the reviewer's suggestion.

> *(2) In abstract, the final sentence is ambitious but heavy. It may benefit from being split into two shorter sentences, for example:*
>
> *"These findings establish RNA as a potent, context-dependent modulator of both virulent amyloids and host-defense peptides. They further reveal phase transitions as tunable regulators of peptide activity and potential therapeutic targets across infectious and neurodegenerative diseases."*

As part of the broader abstract revision, the final sentence was restructured and the abstract as a whole was rewritten to improve clarity and readability, in the spirit of the reviewer's recommendation.

> *(3) In the Introduction section,*
>
> *The phenol-soluble modulins (PSMs) produced by Staphylococci contain amyloid-forming short peptides which play multiple functional roles...", consider "Staphylococcal phenolsoluble modulins (PSMs) are short, amyloidogenic peptides that perform multiple roles central to pathogenesis....*

In accordance with the suggestion, the sentence has been revised.

> *(4) To improve narrative flow in the final paragraph of the Introduction, a short bridging sentence could be added, such as:*
>
> *"Given these nucleic acid interactions, we next examined whether RNA can drive phase separation or structural reorganization of these amyloidogenic peptides."*

We thank the reviewer for this helpful suggestion. It provided an opportunity to clarify an important distinction between the two peptides studied. While LL-37 can self-assemble into higher-order α-helical structures, it is not amyloidogenic, in contrast to PSMα3. We therefore revised the bridging sentence in the final paragraph of the Introduction to read: “Given their shared cationic, amphipathic α-helical character, but distinct amyloidogenic properties, we sought to examine whether RNA differentially influences the assembly landscapes and bioactivity of PSMα3 and LL-37. “

> *(5) The rationale for selecting Poly(A) and Poly(AU) would benefit from further clarification. It would be helpful to specify whether these RNAs are intended to model particular host or bacterial RNA species, such as AU-rich elements, rRNA-like sequences, or mRNA-like contexts.*

Poly(A) and Poly(AU) RNAs were selected as simplified, well-defined model RNAs to probe general peptide–RNA interactions in an unbiased manner, as no prior information was available regarding whether such interactions occur or which specific RNA species might be involved. This rationale is now clarified in the revised text (lines 128–131).

These RNAs are not intended to represent a single biological transcript, but rather generic RNA features relevant to both host and bacterial contexts, including single-stranded homopolymeric regions and AU-rich elements commonly found in mRNAs and stress srelated RNAs. The use of such reductionist RNA models to study RNA–protein interactions, phase behavior, and RNA-modulated aggregation is well established. We nevertheless agree that RNA sequence and structure may influence peptide assembly and activity, and future studies will address sequence-specific and biologically derived RNAs.

> *(6) In Figure 1A, essential EMSA controls- RNA alone, peptide alone, and a nonspecific peptide or PSMα3 should be included to distinguish specific complexes from artifacts, even if presented in the supplementary information. In addition, a competition assay using unlabeled RNA would help confirm binding specificity and rule out predominantly nonspecific electrostatic interactions; these data could also be reported in the supplementary figures.*

An RNA-alone control is already included in Figure 1A of the revised version. The first lane ("0 μM") shows free Poly(A) or Poly(AU) RNA in the absence of peptide and serves as the negative control against which PSMα3-induced mobility shifts are evaluated. A peptide-alone EMSA cannot be performed, as PSMα3 is highly cationic and does not migrate into the gel in the absence of RNA; moreover, EMSA in this format reports on RNA mobility rather than peptide migration.

With respect to binding specificity, we compared Poly(A) and Poly(AU) RNAs and observed distinct binding behaviors, which would not be expected for purely nonspecific electrostatic interactions. In addition, the extracted Hill coefficients (>1) are consistent with cooperative binding, further arguing against simple charge-driven association. Finally, the RNA-dependent association of PSMα3 is independently supported by fluorescence microscopy and quantitative colocalization analyses, which corroborate the EMSA results. Together, these orthogonal approaches support the relevance of the observed peptide–RNA interactions.

> *(7) In Figure 1B, there is a time mismatch between EMSA (30 minutes) and TEM (2 hours). If aggregation progresses over time, the EMSA pattern at 2 hours may differ. This point could be acknowledged or experimentally addressed, as RNA-peptide assemblies may evolve from liquid-like condensates to more solid aggregates.*

The EMSA and TEM experiments were intentionally performed at different time points to capture distinct stages of the PSMα3–RNA assembly process. The EMSA assay (30 minutes) was designed to probe early RNA–peptide complex formation and binding interactions, before extensive higher-order aggregation occurs. At this stage, we aim to detect mobility shifts reflecting complex formation rather than mature assemblies. In contrast, TEM was performed after 2 hours to visualize later-stage structural outcomes, including fibrillation and morphological reorganization. As aggregation progresses over time, the assemblies evolve from early RNA–peptide complexes into more ordered fibrillar structures, which are best assessed by electron microscopy at later time points. To improve clarity and avoid potential confusion, we have streamlined Figure 1 to focus on the EMSA data, which specifically addresses early binding events. The TEM data were removed from Figure 1 and are now presented in Figure 3, where later-stage structural transitions and fibrillation are shown more comprehensively and in the appropriate mechanistic context.

> *(8) In Figure 1B, if feasible, complementing TEM with a confirmatory fibril assay (e.g., ThT kinetics) under the same conditions would strengthen the conclusion that the morphology difference is robust, but it is not mandatory.*

We attempted to perform ThT fibrillation kinetics under the same RNA containing conditions; however, these assays were not informative for this system. PSMα3 aggregates extremely

rapidly, producing an immediate and steep increase in ThT fluorescence (Fig. S9 in the revised version), which prevents reliable resolution of RNA dependent differences in aggregation kinetics or lag phases. In addition, Poly(AU) RNA interferes with ThT readout through electrostatic interactions between the negatively charged RNA and the cationic dye, as well as through RNA-induced changes in fibril morphology, both of which complicate quantitative interpretation of fluorescence kinetics. Based on these technical constraints and prior experience with RNA–amyloid systems, ThT kinetics under identical RNA conditions would not provide a robust or interpretable confirmation of the morphological differences observed by TEM.

> *(9) In Figure 1B, PSMα3 alone control is missing in TEM images.*

A TEM image of PSMα3 alone is included in Figure 3, where we systematically present fibrillation outcomes across different RNA concentrations alongside the peptide-only control. Figure 1 was streamlined to focus on early RNA– peptide interactions assessed by EMSA, whereas Figure 3 provides a comprehensive TEM analysis of later-stage structural outcomes. This organization was chosen to clearly separate early binding events from subsequent assembly transitions and to avoid redundant presentation of TEM images under similar conditions.

> *(10) Although it is experimentally practical to focus on Poly(AU), the justification is very one-sided. The Poly(A) condition, which yields amorphous aggregates, may be equally informative for understanding toxicity, LLPS, or nonfibrillar states and could be discussed more explicitly.*

We agree that Poly(A)-induced amorphous aggregation is informative for understanding non fibrillar assembly states. However, the primary aim of this study was to dissect RNA-dependent regulation of fibrillar assembly and phase behavior, which is most clearly captured using Poly(AU). Poly(A) was therefore included as a comparative condition rather than as a focus for detailed mechanistic analysis. A more systematic comparison of different RNA classes and their effects on non fibrillar states and toxicity is an important direction for future work but is beyond the scope of the present study.

> *(11) To improve readability of the manuscript, the main text should follow the order of the figure panels (e.g., A, B, C, D, and E) and numbers (Figure 1, 2...) sequentially, so that readers can easily align with the corresponding images.*

We have revised the manuscript to improve alignment between the main text and the figures, adjusting panel ordering and numbering where appropriate so that the text now follows the figure panels and figure numbers more sequentially. These changes were made to enhance readability while maintaining a logical visual flow within the figures.

> *(12) In the result section of Figure 2, the analogy to Ddx4-like systems is a helpful concept, but should be clearly framed as an analogy, not evidence. It would be more accurate to say that the behavior is "conceptually similar to" those systems, while noting that the molecular context is significantly different.*

We have revised the text to explicitly frame the comparison to Ddx4-like systems as a conceptual analogy rather than evidence: lines 158-161 in the revised version.

> *(13) In Figure 4, inclusion of positive and negative controls to validate assay performance (e.g., untreated bacteria or HeLa cells, lysis buffer, media alone) would strengthen confidence in the bioactivity measurements.*

We wish to clarify that appropriate positive and negative controls were included in all bioactivity assays and were used to normalize the data presented in Figure 4. For the HeLa cytotoxicity assay (LDH), untreated cells were used to determine spontaneous LDH release

(negative control), and cells treated with the manufacturer supplied lysis buffer were used to determine maximum LDH release (positive control). The percent cytotoxicity shown in Figure 4B was calculated relative to these internal controls, as described in the Methods. For the antibacterial assay (PrestoBlue), wells containing *E. coli* without peptide served as the positive control for 100% viability, while wells containing sterile LB medium alone were used as blanks. Viability values in Figure 4A were normalized to these controls. We have ensured that the Methods section explicitly describes these controls to reinforce confidence in the bioactivity measurements.

> *(14) To enhance clarity, consider presenting the RNA concentration and time-dependent effects on PSMα3 bioactivity in a comparison table within the main text or as a supplementary figure.*

We appreciate this suggestion and carefully considered presenting the data in tabular form. However, we found that graphical representation more effectively conveys the trends, transitions, and comparative patterns between conditions. A table would not adequately capture these relationships.

> ***Reviewer #2 (Recommendations for the authors):***
>
> *Further remarks:*
>
> *(1) Circumstantial evidence based on the "amyloid inhibitor", EGCG: The results with EGCG, which has been shown to have a moderate amyloid-reducing effect on PSMalpha 1 and PSMalpha4, should not be taken as evidence for amyloid-based cytotoxicity. While increased concentrations of EGCG reduced the cytotoxic effect of PSMalpha3, it is not convincingly shown that this is due to a lower concentration of amyloid vs. monomeric PSM.*

We agree that the effects of EGCG should not be interpreted as evidence for amyloid fibrils being the cytotoxic species. Our data instead support a mechanism in which EGCG primarily targets soluble PSMα3, thereby redirecting its assembly pathway and depleting bioactive species. Specifically, solution-state NMR (Fig. 7) shows that EGCG binds defined residues of monomeric PSMα3, consistent with sequestration of soluble peptide rather than selective inhibition of fibrils. Complementary light and electron microscopy, together with kinetic measurements, indicate that EGCG does not simply stabilize monomers but instead diverts PSMα3 into amorphous, non-functional aggregates, as visualized by TEM (Fig. 6B) and reflected in altered ThT responses (Fig. S9). Importantly, these EGCG-induced aggregates are non-cytotoxic (Fig. 6A/C) and fail to associate with membranes or cells, in contrast to untreated PSMα3, which forms membrane-associated assemblies and induces disruption (newly added Movies S1-S2). Thus, EGCG potentially reduces cytotoxicity by remodeling the aggregation landscape and depleting active soluble species, rather than by selectively inhibiting specific fibril formation. This clarification is now added to the Discussion in lines 554-564 of the revised version.

> *(2) It is appreciated that the authors refrain from presenting the unsubstantiated concept of "functional" PSM amyloids in the discussion. However, wording in that direction must also be removed from other parts of the manuscript (e.g. "bioactive fibrillar polymorphs". "The formation of cross-alpha amyloids has been correlated with toxic activity", etc.), generally refraining from uncritically implying that amyloid formation underlies PSM biological activity, and rather discussing that the much more likely explanation of the findings is a lowering of cytolytically active, monomeric PSM concentration.*

As detailed in our response to Major Comment #1, we agree that uncritical language implying that amyloid fibrils themselves are the cytotoxic species should be avoided. Accordingly, we

have revised the manuscript to consistently frame amyloid formation in regulatory terms. Aggregation, depending on context, modulates activity by altering the availability, persistence, and assembly pathways of these species. Distinct aggregation states are therefore presented as correlated with, but not equivalent to, cytotoxic activity, and as components of a dynamic assembly landscape rather than as direct toxic entities.

> *(3) Discussion: "PSM alpha3 interaction with nucleic acids within human cells ...supports a comparable mechanism...". Please delete this as it is unsubstantiated.*

We agree that the original phrasing overstated the evidence. The sentence was removed and the Discussion was revised to clearly frame nucleolar accumulation as a phenomenological observation reflecting PSMα3's intrinsic nucleic acid–binding capacity, rather than as evidence for a comparable intracellular mechanism. Specifically, the revised Discussion (lines 597–607) states that nucleolar localization is "unlikely to represent a distinct intracellular toxic mechanism" and instead "reflects binding competence within RNA-rich compartments following cellular entry." The biological relevance of this interaction, particularly at sub-cytotoxic concentrations, is noted as an open question requiring further investigation.

> *(4) The authors should also cite papers that have argued against their central hypothesis of "functional" PSM amyloids.*

We thank the reviewer for this suggestion. Accordingly, we have revised the manuscript to explicitly cite and discuss studies that argue against amyloid fibrils as the primary cytotoxic species, and that instead attribute PSM cytotoxicity to soluble or membrane-associated forms. These perspectives are now incorporated in the Discussion to provide a balanced view of the field and to clarify how our findings align with, and differ from, existing models of PSM activity.

https://doi.org/10.7554/eLife.109290.2.sa0